

1 **Authigenesis of biomorphic apatite particles from Benguela upwelling zone sediments off**  
2 **Namibia: The role of organic matter in sedimentary apatite nucleation and growth**

3 Kaarel Mänd<sup>1,2\*</sup>, Kalle Kirsimäe<sup>2</sup>, Aivo Lepland<sup>2,3,4,5</sup>, Chris H. Crosby<sup>6</sup>, Jake V. Bailey<sup>6</sup>, Kurt O.  
4 Konhauser<sup>1</sup>, Richard Wirth<sup>7</sup>, Anja Schreiber<sup>7</sup>, and Kaarel Lumiste<sup>2</sup>

5 <sup>1</sup>Department of Earth and Atmospheric Sciences, University of Alberta, Edmonton T6G 2E3,  
6 Canada

7 <sup>2</sup>Department of Geology, University of Tartu, Ravila 14A, 50411 Tartu, Estonia

8 <sup>3</sup>CAGE – Centre for Arctic Gas Hydrate, Environment and Climate, Department of Geosciences,  
9 UiT The Arctic University of Norway, 9037 Tromsø, Norway

10 <sup>4</sup>Geological Survey of Norway, 7491 Trondheim, Norway

11 <sup>5</sup>Institute of Geology, Tallinn University of Technology, 19086 Tallinn, Estonia

12 <sup>6</sup>Department of Earth Sciences, University of Minnesota–Twin Cities, Minneapolis, 55455, USA

13 <sup>7</sup>GFZ German Research Centre for Geosciences, Section 4.3: Chemistry and Physics of Earth  
14 Materials, Telegrafenberg, 14473 Potsdam, Germany

15 \* Corresponding author: kaarel.mand@ualberta.ca; 1-26 Earth Sciences Building, University of  
16 Alberta, Edmonton, Alberta, Canada T6G 2E3

17

18 **Abstract**

19 Sedimentary phosphorites comprise a major phosphorus (P) ore, yet their formation remains  
20 poorly understood. Extant polyphosphate-metabolizing bacterial communities are known to act as  
21 bacterial phosphate-pumps, leading to episodically high dissolved phosphate concentrations in  
22 pore waters of organic-rich sediment. These conditions can promote the precipitation of  
23 amorphous precursor phases that are quickly converted to apatite – usually in carbonate  
24 fluorapatite form  $[Ca_{10}(PO_4,CO_3)_6F_{2-3}]$ . To assess the mechanisms underpinning the nucleation  
25 and growth of sedimentary apatite, we sampled P-rich sediments from the Namibian shelf, a

26 modern environment where phosphogenesis presently occurs. The P-rich fraction of the topmost  
27 centimeters of sediment mainly consists of pellets about 50 to 400  $\mu\text{m}$  in size, which in turn, are  
28 comprised of micron-sized apatite particles that are often arranged into radial structures with  
29 diameters ranging from 2 to 4  $\mu\text{m}$ , and morphologies that range from rod-shapes to dumbbells to  
30 spheres that resemble laboratory-grown fluorapatite-gelatin nanocomposites known from double-  
31 diffusion experiments in organic matrices. The nucleation and growth of authigenic apatite on the  
32 Namibian shelf is likely analogous to these laboratory-produced precipitates, where organic  
33 macromolecules play a central role in apatite nucleation and growth. The high density of apatite  
34 nucleation sites within the pellets ( $>10^9$  particles per  $\text{cm}^3$ ) suggests precipitation at high pore  
35 water phosphate concentrations that have been reported from the Namibian shelf and may be  
36 attributed to microbial phosphate pumping. The intimate association of organic material with the  
37 apatite could suggest a possible role of biological substrata, such as exopolymeric substances  
38 (EPS), in the nucleation of apatite precursors. Importantly, we do not observe any evidence that  
39 the apatite particles are actual phosphatized microbes, contradicting some earlier studies.  
40 Nevertheless, these results further evidence the potential importance of microbially-derived  
41 (extracellular) organic matter as a template for phosphatic mineral nucleation in both recent and  
42 ancient phosphorites.

43

## 44 **Introduction**

45 Phosphorites – rocks that contain  $>9$  wt.%  $\text{P}_2\text{O}_5$  (Filippelli, 2011) – constitute the largest sink of  
46 sedimentary phosphorus (Delaney, 1998). Not only do they remove P from the global

47 biogeochemical cycle, but importantly, they influence Earth's primary production on geological  
48 time scales (Tyrrell, 1999). Phosphorites are also a critical non-renewable resource for  
49 agriculture, specifically required in the production of phosphatic fertilizer (Cordell *et al.*, 2009).  
50 However, despite their economic importance, the origin of these mineral deposits remains  
51 enigmatic.

52         The main sites of modern phosphorite formation are major upwelling systems along  
53 continental margins where primary production and the flux of sinking organic matter – and thus  
54 of P – to the seafloor are relatively high. Indeed, the great majority of modern phosphorites form  
55 today in regions of upwelling (Föllmi, 1996), such as on the western coasts of Namibia  
56 (Summerhayes *et al.*, 1973; Baturin & Bezrukov, 1979; Baturin, 2000; Compton & Bergh, 2016),  
57 Chile and Peru (Veeh *et al.*, 1973; Burnett, 1977; Burnett *et al.*, 2000), Mexico (Jahnke *et al.*,  
58 1983; Schuffert *et al.*, 1998), and in the Arabian Sea (Schenau *et al.*, 2000), with some  
59 exceptions, such as off-shore eastern Australia (O'Brien & Veeh, 1980; O'Brien & Heggie,  
60 1988).

61         The processes necessary for the formation of sedimentary phosphorites begin with  
62 weathering of P-bearing minerals, solubilization to the phosphate anion ( $\text{PO}_4^{3-}$ ), and transport by  
63 rivers and groundwater to the oceans. Once in seawater, P is rapidly incorporated into biomass or  
64 adsorbed to Fe/Mn-oxyhydroxides, both of which are eventually deposited on the seafloor.  
65 Heterotrophs take advantage of the high flux of easily degradable organic matter, resulting in  
66 oxygen levels in the bottom waters that are low enough to cause a steep (sub)oxic-sulfidic  
67 redoxcline in the shallow sediment subsurface. In addition to remineralization of organic matter,

68 these conditions also facilitate redox-sensitive reactions, such as polyphosphate cycling by sulfur-  
69 oxidizing bacteria (Schulz & Schulz, 2005) and, to a lesser degree, the reductive dissolution of  
70 Fe/Mn-oxyhydroxides (Noffke *et al.*, 2012). These processes all result in the release of phosphate  
71 anions into sediment pore waters, which may eventually lead to supersaturation with respect to  
72 amorphous apatite precursor phases, and ultimately the transformation into the stable crystalline  
73 phase, carbonate fluorapatite (Föllmi, 1996; Goldhammer *et al.*, 2010; Filippelli, 2011;  
74 Ruttenberg, 2014).

75         Dissolved phosphate concentrations in pore waters of the topmost few centimeters of  
76 organic-rich sediment can reach >400  $\mu\text{M}$ , and thus exceed the solubility product of amorphous  
77 apatite precursors (Krajewski *et al.*, 1994; Schulz & Schulz, 2005; Goldhammer *et al.*, 2011;  
78 Dale *et al.*, 2013). While sinking organic matter is the main source of P in the sediments, and a  
79 large flux is a prerequisite for the formation of phosphorites, it has been shown that simple  
80 remineralization of organic matter by heterotrophs is on its own not enough to produce the  
81 observed concentrations of dissolved phosphate in sediment pore waters (Froelich *et al.*, 1988;  
82 Krajewski *et al.*, 1994). Furthermore, Fe input into sediments in upwelling environments has  
83 been found to be low, precluding a significant role of redox-dependent Fe cycling in increasing  
84 phosphate concentrations (Brüchert *et al.*, 2006; Noffke *et al.*, 2012). In this regard, several  
85 studies have recently highlighted the catalytic role that microbial processes play in mediating  
86 apatite precipitation (Schulz & Schulz, 2005; Arning *et al.*, 2008, 2009a; Goldhammer *et al.*,  
87 2010; Brock & Schulz-Vogt, 2011). For instance, several genera of sulfur-oxidizing bacteria have  
88 been demonstrated to store intracellular polyphosphate granules (*e.g.*, *Beggiatoa*, *Thiomargarita*).  
89 Steep (sub)oxic-sulfidic redoxcline conditions are known to provide a habitat for some

90 phosphate-cycling chemolithoautotrophs, which act as “phosphate pumps”. These bacteria are  
91 capable of accumulating polyphosphate intracellularly under oxic and suboxic conditions, then  
92 hydrolyzing the polyphosphate and releasing phosphate under sulfidic conditions in short, but  
93 intense, pulses (Froelich *et al.*, 1988; Föllmi, 1996; Schulz & Schulz, 2005; Goldhammer *et al.*,  
94 2010; Holmkvist *et al.*, 2010; Brock & Schulz-Vogt, 2011). For example, in the case of the  
95 phosphogenic Namibian shelf, Schulz & Schulz (2005) found that, in a 3-cm thick horizon below  
96 the sediment-water interface, peak *Thiomargarita* abundance coincided with a peak in dissolved  
97 phosphate concentration (>300  $\mu\text{M}$ ) and in hydroxyapatite abundance in the solid phase of the  
98 sediment. This mechanism suggests that sufficiently high bacterial phosphate “pumping” rates  
99 can lead to intermittent supersaturation of pore water with respect to carbonate fluorapatite  
100 precursors (Arning *et al.*, 2009b; Goldhammer *et al.*, 2010).

101 In addition to supersaturation, for mineral formation to occur, the activation energy  
102 barriers to nucleation need to be overcome. Previous experiments that investigated the  
103 precipitation of phosphate minerals have demonstrated that direct precipitation of apatite from  
104 supersaturated solution is a very slow process (Krajewski *et al.*, 1994; Golubev *et al.*, 1999;  
105 Gunnars *et al.*, 2004). Instead, at sufficiently high levels of supersaturation, more soluble  
106 amorphous phases of calcium phosphate, such as octacalcium phosphate (Brown *et al.*, 1984;  
107 Gunnars *et al.*, 2004) or amorphous calcium phosphate (Martens & Harriss, 1970; Golubev et al.,  
108 1999), begin to nucleate at a much higher rate due to the significantly lower activation energy  
109 barriers to nucleation for these phases. The amorphous phases then serve as precursor sites for  
110 apatite nucleation and growth (van Cappellen & Berner, 1991; Krajewski *et al.*, 1994; Schenau *et*  
111 *al.*, 2000; Golubev et al., 1999; Gunnars *et al.*, 2004; Borkiewicz *et al.*, 2010; Oxmann &

112 Schwendenmann, 2014). It is plausible that sedimentary bacteria and/or microbially produced  
113 organic compounds, such as exopolymeric substances (EPS), may also serve as substrata for  
114 nucleation, thus enhancing phosphate precipitation. Experiments aimed at investigating microbial  
115 biomineralization show that apatite group minerals can preferentially precipitate on bacterial  
116 sheaths and cell walls (*e.g.*, Benzerara *et al.*, 2004), though earlier studies downplay the role of  
117 such substrata in the rapid precipitation of apatite precursor phases (*e.g.*, Hirschler *et al.*, 1990;  
118 Krajewski *et al.*, 1994).

119           Despite much experimental work, what remains to be determined is whether the  
120 experiments represent natural conditions, especially with respect to the influence of organic  
121 substrata. In this regard, an ideal study site for the evaluation of the mechanisms underpinning  
122 phosphate precipitation are the phosphorites that are currently still forming on the Namibian  
123 continental shelf – a site of considerable controversy over phosphorite mining plans, with  
124 uncertain implications for the local marine ecosystem (Midgley, 2012; Watson *et al.*, 2014).  
125 Previous studies of this location have suggested that phosphate precipitation is microbially  
126 influenced (Schulz & Schulz, 2005) and that the physical concentration of apatitic pellets may be  
127 due to sediment reworking caused by changes in sea level (Compton & Bergh, 2016).  
128 Accordingly, the aim of this work was to study the micro- and nanofabric of those same  
129 phosphorites to better understand how sedimentary authigenic apatite forms, and whether the  
130 phosphogenesis fossilizes microbial structures.

131

## 132 **Geological setting**

133 The Namibian shelf is known for its unusual breadth and depth, extending to 400 m water depth.  
134 It consists of Proterozoic to Cenozoic basement rocks and a thin Cenozoic sedimentary  
135 succession, terminated by an erosional surface on which late Cenozoic to modern sediments were  
136 deposited (Compton & Bergh, 2016). The Namibian shelf is influenced by the Benguela  
137 Upwelling System, representing some of the strongest upwelling currents in the world. The rising  
138 nutrient-rich deep ocean waters fuel the world's most biologically productive eastern boundary  
139 marine ecosystem (Carr, 2001), which is associated with intense organic carbon burial (Inthorn *et*  
140 *al.*, 2006). Combined with a modest detrital input (Eckardt & Kuring, 2005), the prolific algal  
141 production has led to the accumulation of an up to 15 m thick layer of Pleistocene to modern  
142 diatomaceous mud near Walvis Bay (Figure 1; Baturin, 2000). This mud grades into less  
143 diatomaceous organic-rich mud towards the south. The nearshore shelf sediments tend to consist  
144 of sand and gravel, while the outer shelf hosts carbonates (Figure 1; Compton & Bergh, 2016).

145         Remineralization of the high flux of sinking organic matter in the coastal upwelling  
146 system off Namibia creates fluctuating shelf anoxia and sulfidic water-column conditions,  
147 titrating the limited Fe input (Brüchert *et al.*, 2006) and further decreasing the importance of Fe-  
148 Mn oxyhydroxides in P cycling. The organic matter also acts to deliver P to the sediments – a  
149 primary factor enabling the formation of phosphorites on the inner shelf – while the fluctuating  
150 redox conditions facilitate phosphogenic polyphosphate metabolism, driving phosphate  
151 concentrations in the pore waters up to levels required for apatite precursor precipitation (Schulz  
152 & Schulz, 2005; Brock & Schulz-Vogt, 2011). Phosphorite deposits range in age from late

153 Oligocene to modern (late Miocene to modern off the Namibian coast), and geographically they  
154 extend from the southern shelf of South Africa up to the Kunene River. The modern locus of  
155 phosphogenesis has, however, shifted northwards since the Pleistocene, to the diatomaceous  
156 mudbelt near Walvis Bay (Baturin, 2000; Compton *et al.*, 2002, 2004; Compton & Bergh, 2016).  
157 These phosphorites usually occur in the form of apatitic pellets, which are typically a few  
158 hundred micrometers in diameter, along with concretionary authigenic forms, phosphatized  
159 mollusk molds and occasional recent phosphatic brachiopods (Baturin, 2000).

160           Based on petrologic features, Namibian phosphorites can broadly be divided into two  
161 classes: (i) dispersed, authigenic Pleistocene to modern phosphatic concretions and pellets that  
162 are still forming in the diatomaceous mud of the inner shelf, at water depth ranges between 50  
163 and 140 m (whole sediment P<sub>2</sub>O<sub>5</sub> content ~0.8 wt.%; Veeh *et al.*, 1974; Baturin, 2000) and (ii)  
164 reworked, late Miocene to Pleistocene-aged phosphatic sediments occurring as P-rich lags on the  
165 middle to outer shelf at 180 to 500 m water depth, consisting of a 1–2 m thick P-rich layer, which  
166 displays a coarsening upward succession from muddy to increasingly more sandy and gravelly  
167 sediment (average P<sub>2</sub>O<sub>5</sub> content 19 wt.%; Compton and Bergh, 2016). Aside from phosphorite  
168 sand, skeletal fish debris, foraminifera and bivalve shells and terrigenous components co-occur in  
169 the sediment pile. Strontium isotope stratigraphy places the formation time of this phosphorite  
170 from the late Miocene to Pleistocene, beginning at roughly 5.8 Ma, with the majority of the  
171 deposit having formed during the Pliocene and Pleistocene (Compton & Bergh, 2016). Some  
172 pellets show evidence of zonation consistent with multiple episodes of phosphorite formation;  
173 this, in addition to the sedimentary fabric and different strontium isotope ratios for pellets in the  
174 same sample, points to complex sedimentary reworking. Compton and Bergh (2016) explain the



175 formation of this deposit through changes in sea level that has resulted in the reworking, transport  
176 and concentration of previously-formed authigenic phosphorite from the diatomaceous mudbelt  
177 to sediments further offshore, similar to what has previously been reported for South African  
178 deposits (Compton *et al.*, 2002, 2004; Wigley & Compton, 2006). Authigenic phosphorite  
179 formation is interpreted to have taken place during sea level highstands and reworking during  
180 lowstands, beginning with the onset of glacial cycles in the Pleistocene (Compton & Bergh,  
181 2016). During sampling, none of the coring sites chosen for their location at known areas of  
182 phosphorite abundance yielded any phosphorite, while those that did were taken from areas  
183 assumed to be low in P content, reflecting the patchy occurrence of phosphorites on the Namibian  
184 shelf (Figure 1).

185

## 186 **Materials and methods**

187 The sediment samples used for this study were collected during oceanographic cruises on the  
188 research vessel *Mirabilis* in the central-southern shelf sea off the coast of Namibia in May of  
189 2015. An Ocean Instruments MC-400 multi-corer was used to sample a variety of unconsolidated  
190 sediments, of which two cores were used in this study – core GC4 (21 cm in length, from ~300 m  
191 water depth) and core 25005 (25 cm in length, from ~50 m water depth) (Figure 1). The top 10  
192 cm of the cores were sectioned and sampled at 1 cm intervals; below that, the intervals were 2 cm  
193 in length. The bottom waters and topmost centimeters of sediment sampled by the multi-corer did  
194 not smell of H<sub>2</sub>S, indicating oxic or suboxic conditions at the sediment-water interface at the time  
195 of sampling. The samples were freeze dried following collection. While this process is likely to

196 affect the preservation of amorphous microstructures with high water contents, such as biofilms  
197 and other organic substrata, already crystallized apatite structures are not affected, especially if  
198 these are seen to still preserve a fine-grained primary microfabric.

199           The mineralogical composition of whole rock samples was studied by X-ray  
200 diffractometry (XRD) at the University of Tartu, Estonia. Samples were pulverized by hand with  
201 an agate pestle and mortar and unoriented preparations were made. Powders were then scanned  
202 on a Bruker D8 Advance diffractometer using Cu K $\alpha$  radiation and LynxEye positive sensitive  
203 detector in 2–70° 2 $\Theta$  range. The mineralogical composition of each sample, along with their  
204 apatite lattice parameters, were interpreted and modeled using the Rietveld algorithm-based  
205 program Topaz. Total organic carbon content of core GC4 was estimated by measuring the mass  
206 lost on heating several dried GC4 samples at 500°C for 24 hours. Solid-phase P and S  
207 concentrations of the sediments in core 25005 were determined using inductively coupled plasma  
208 mass-spectrometry (ICP-MS) in multi-acid digested (HNO<sub>3</sub>, HClO<sub>4</sub>, HF, HCl) samples at Bureau  
209 Veritas Commodities Canada Ltd in Vancouver.

210           To specifically study the microstructure, several 100–400  $\mu$ m apatitic pellets were  
211 handpicked from bulk samples under a microscope. Impurities of lighter minerals and high  
212 porosity did not allow heavy liquid fractionation of the apatitic pellets. The preparation of the  
213 pellets was done either by (i) cleaning in an ultrasonic bath, mounting on an adhesive carbon  
214 film, and breaking with a scalpel to reveal their inner structure, or (ii) embedding in epoxy resin,  
215 then finely grinding down to reveal a cross-section. The polished samples were subsequently

216 milled at the University of Tartu with a Leica EMRES101 Wide Beam Argon Ion Mill to produce  
217 a smooth and clean flat surface.

218 For micromorphology studies, the polished pellets were coated with a few nm thick  
219 conductive carbon layer, while broken surfaces were coated in platinum. Scanning electron  
220 microscope (SEM) imaging was performed using a variable pressure Zeiss EVO MA15 SEM  
221 equipped with Oxford X-MAX energy dispersive detector system (EDX) and AZTEC software  
222 for element analysis at the University of Tartu; and Zeiss Sigma 300 VP-FESEM equipped  
223 Bruker EDX at University of Alberta, Canada. Imaging was done both in back-scattered electron  
224 (BSE) and secondary electron (SE) modes.

225 Selected cross-sections of apatitic pellets were investigated using transmission electron  
226 microscopy (TEM). The 15 x 5 x 0.15  $\mu\text{m}$  foils for TEM study were cut from embedded and  
227 polished samples using Focused Ion Beam (FIB) technique on a FEI FIB200-TEM at  
228 GeoForschungsZentrum Potsdam, Germany (locations of the cuts are shown on Figure S1). The  
229 foils were mounted on a lacy carbon film and examined with a FEI Tecnai G2 F20 X-TWIN  
230 TEM operated at 200 kV with a field emission gun as electron source. The TEM imaging and  
231 analysis were done using a Fishione high-angle annular dark-field detector (HAADF), Gatan  
232 imaging filter (GIF) Tridiem and EDAX X-ray analyzer with ultra-thin window. Analytical data  
233 were processed using the TIA software package. Electron energy-loss (EELS) element maps were  
234 performed with C-K and S-K edges using the jump-ratio technique.

235 The laboratory-grown apatite pseudofossils shown in Figure 10 were precipitated in the  
236 diffusion gel portion of a double diffusion gradient setup, designed to mimic Ca, F and  $\text{PO}_4^{3-}$

237 interaction in sediment pore water conditions (Crosby & Bailey, 2017). The precipitates  
238 suspended in the gel were then removed from the diffusion setup, residue gel dissolved in water,  
239 and concentrated precipitates mounted on an adhesive carbon film on top of an SEM stub.  
240 Imaging was done on a Hitachi TM1000 Tabletop ESEM operated at 15.0 kV accelerating  
241 voltage, and analyzed by EDS using Bruker Quantax 50 software (Crosby & Bailey, 2018).

242

## 243 **Results**

### 244 **Mineralogy and chemistry**

245 Sediments in core GC4 are enriched in organic matter (up to 10–15 wt.%). The sediments can be  
246 described as calcareous phosphatic sands (Figure 2a), containing mostly calcite, quartz, some  
247 phyllosilicates (glauconite) and abundant apatite (Figure 3a). The content of apatite is relatively  
248 uniform (ca. 19–28 wt.%) throughout the core, rising slightly towards the bottom (Figure 3c).

249 Sediments in core 25005 are rich in opalinous diatom frustules (Figure 2b). Mineral  
250 composition of the sediment is characterized by quartz, plagioclase, K-feldspar, calcite and  
251 glauconite (Figure 3a). Elevated levels of apatite were identified in the upper half of the core  
252 down to 8 cm depth, with the highest relative amount (up to 11 wt.%) found at 6 cm depth  
253 (Figure 3a). Apatite nearly disappears in the lower part of the core, coincident with the  
254 appearance of pyrite (Figure 3d). The distributions of apatite and pyrite determined by X-ray  
255 diffraction are consistent with the chemical composition of the sediment, showing a peak in P

256 concentration of 1.9 wt.% at 5 cm of depth, dropping below 0.3 wt.% deeper in the core, while S  
257 content rises from near-zero values to 0.6 wt.% over the same interval (Figure 3e).

258           The apatite can be identified by its characteristic XRD pattern as a carbonate fluorapatite  
259 mineral. It is poorly crystalline, as evident from the low values of apatite coherent stacking  
260 domain sizes which average approximately 31 nm in core GC4 and 23 nm in core 25005. The  
261 unit cell parameters of apatite in core GC4 are well constrained, varying between 9.327 and 9.332  
262  $\pm 0.002$  Å and 6.885 and 6.889  $\pm 0.002$  Å for *a* and *c* parameters, respectively (Figure 3b). These  
263 values fall within the field ascribed to sedimentary phosphorites. However, the unit cell  
264 parameters of apatite in core 25005 have a much larger variance than in GC4 – between 9.298  
265 and 9.337  $\pm 0.005$  Å for *a* parameter and between 6.865 and 6.900  $\pm 0.007$  Å for *c* parameter, and  
266 hence, they are significantly outside the range of most sedimentary phosphorites. This is possibly  
267 due to a more poorly ordered crystal structure with a higher number of defects (Figure 3b).

268

## 269 **Microscopy**

270 Under optical microscopy and SEM, samples from both cores were found to be dominated by  
271 aggregates of mud and organic debris with abundant diatom frustules. In addition, there are  
272 ostracod valves and other calcareous shelly fragments, quartz, feldspar and glauconite grains, a  
273 small fraction of heavy minerals, and numerous apatitic pellets (Figures 4a, b). The average grain  
274 size of the particulate fraction is typically between 100 to 300  $\mu\text{m}$ .

275           Apatitic pellets appear under optical microscopy as dark gray to black in color and are  
276 slightly larger compared to other grains. The surfaces of the pellets are usually splotchy and

277 pitted. SEM reveals that most of the studied pellets in the core GC4 are ~200 to 400  $\mu\text{m}$  in  
278 diameter and are rounded or slightly flattened with smooth surfaces (Figure 4c). In core 25005,  
279 the pellets typically measure 50 to 300  $\mu\text{m}$  in diameter, and have a more pitted surface. These are  
280 poorly- to well-rounded and generally elongated (Figure 4d), with numerous pits or pores that  
281 open to the pellet surface.

282         At a broken surface, most pellets are composed of a porous apatite aggregate embedding  
283 fragments of fossil remains, commonly diatom frustules, as well as terrigenous grains. Fossil  
284 detritus is most abundant in pellets from core 25005, but rare in pellets from GC4 where the  
285 detritus has mostly been dissolved and only casts remain (Figures 4e–f). Pellets show variable  
286 porosity, whereas some of the pores represent either hollow spaces inside well-preserved diatom  
287 frustules – suggestive of lumina – or what are possibly dissolved casts of fossils (Figure 4f).  
288 Diameters of pores are tens of  $\mu\text{m}$  or less. Estimated porosity (relative area of the pores in the  
289 pellet’s cross-section) is ~1–2% in pellets from core GC4 and ~3–10% in those from core 25005.  
290 The apatitic pellets also typically have an irregular patchy inner structure (Figures 5a–b).  
291 Backscattered electron images of polished pellets in core GC4 reveal concentric structures  
292 composed of layers ca. 10–20  $\mu\text{m}$  thick (Figure 5a). Also, pellets in core 25005 occasionally  
293 show a single rim at the pellet’s outer perimeter exhibiting a similar concentric-layered  
294 texture (Figure 5b).

295         At higher resolution, the micrographs show that the pellets consist of micron-scale apatite  
296 particles that are often arranged into radial structures with diameters ranging from 2 to 4  $\mu\text{m}$   
297 (Figure 5c). The structural details of the apatite particles are revealed at pore margins and within  
298 pores, where they are shown to consist of various morphologies, including irregular, colloform,

299 globular, dumbbell-shaped, and elongated (Figure 6a). The most typical are elongated, rod-  
300 shaped apatite particles with rounded ends, generally ca. 0.5  $\mu\text{m}$  to 4  $\mu\text{m}$  in length, and  
301 approximately a third of that in diameter (Figure 6b). With few exceptions, the rod-shaped  
302 particles are of similar size within any particular pellet, but can vary in size between different  
303 pellets or cores.

304 The rod-shaped particles are not single apatite crystallites, but instead are composed of  
305 elongated nanocrystallites (tens of nanometers in diameter) which are oriented parallel to the long  
306 axis of the particles. In core 25005, the crystallites composing the rod-shaped particles are  
307 elongated and anhedral in appearance (Figure 6c), but in core GC4, these are larger in size and  
308 possess a distinctly hexagonal morphology characteristic of the apatite crystal habit (Figures 6d,  
309 8b). In most cases, the rod-shaped particles occur together with films or filaments composed of  
310 organic polymeric macromolecules that could possibly represent dried remnants of organic  
311 matrices (e.g., EPS) that have been heavily dehydrated during sample preparation in high  
312 vacuum. The organic substance covers the pore wall wherever there are rod-shaped particles  
313 present, connecting several structures as filaments or sheets (Figure 6e). Often, the rod-shaped  
314 particles also occur together with framboidal pyrite aggregates roughly 0.3 to 3  $\mu\text{m}$  in diameter  
315 (Figure 6f).

316 TEM analysis of foils cut from apatite particles reveal that the rod-shaped particles have a  
317 heterogeneous inner structure (Figure 7) and are composed of several concentric layers about 50–  
318 200 nm thick (Figure 7b). The layers consist of apatite crystallites a few nanometers in diameter.  
319 The contrast between the layers could be due to different porosity (electron transparency) and/or  
320 due to changes in sulfur and carbon content, likely the result of minor incorporation of the

321 organic substance covering the pore walls (Figures 7d–f). Furthermore, the electron diffraction  
322 patterns indicate that the apatite in the inner layers of the rod-shaped particles has greater  
323 crystallinity (i.e. greater long range structural ordering, fewer defects) than in the outer layers,  
324 and that the outer layers show smeared reflections, reminiscent of nanoscale misorientation of  
325 individual crystallites (Figures 7i–j). However, in several cases, highly crystalline, elongated  
326 apatite crystallites are nucleated at the ends of the rod-shaped particles, growing parallel to and/or  
327 radiating along the long axis of concentric rod-shaped particles (Figure 7c).

328           The rod-shaped particles frequently intersect one another, or are intergrown at different  
329 angles and to different degrees (Figure 8a). They can also form larger radially growing  
330 aggregates (Figure 8b). In some rare cases, the rod-shaped particles appear to have nucleated and  
331 grown tangentially on solid surfaces, such as diatom frustules (Figure 8c). Most often, however,  
332 the walls of pores are composed of intergrown rod-shaped particles (Figure 8d). In addition,  
333 progressive growth phases of the rod-shaped particles can be discerned (Figure 9). Rod-shaped  
334 particles (Figure 9a) are joined by dumbbell-like structures, being somewhat larger due to their  
335 bulging distal ends (Figure 8e, 9b–c). Much of the pore walls are also coated with larger  
336 colloform or spherical microstructures (Figure 8f, 9d).

337

### 338 **Apatite double-diffusion experiments**

339 Beginning within ~30h of the start of the double-diffusion experiments, the ion fronts began to  
340 interact and apatite began to precipitate out in a faint band that proceeded to separate into several  
341 distinct zones over the next 4 to 5 days. SEM micrographs reveal that within the gel environment,



342 apatite precipitated in a wide variety of morphologies (Figure 10; reviewed in Crosby & Bailey,  
343 2018). Most of the structures represent either rod-shaped particles (Figure 10a), variously  
344 intersecting dumbbells (Figure 10b, d, e) or closed spheres (Figure 10c). During the later phases  
345 of apatite precipitation, larger spheres, which can develop concentric rims tens of  $\mu\text{m}$  in  
346 thickness, form (Figure 10f).

347

## 348 **Discussion**

### 349 **The phosphogenic system**

350 The phosphatic samples from core GC4 represent a large reworked phosphate sand deposit that  
351 formed during Pleistocene sea-level low-stands in the Namibian middle-to-outer shelf, where  
352 apatite ranges in age from the late Miocene to the Pleistocene (Compton & Bergh, 2016). In  
353 contrast, the organic-rich muddy sediments at site 25005, though outside the typical  
354 diatomaceous mud province around Walvis Bay (Figure 1), are within the zone most affected by  
355 the Benguela Upwelling System and characterized by high organic matter flux. At around 50 m  
356 depth, site 25005 is situated within the reported depth range of authigenic phosphorites. The site  
357 is shallow enough to have been periodically exposed during most of the Pleistocene (Bintanja *et*  
358 *al.*, 2005). However, it is unlikely that the phosphorites at this site are the result of intensive  
359 transport and reworking of preexisting phosphatic deposits (as the relict phosphorite deposits of  
360 the middle to outer shelf are) because the apatitic pellets co-occur with abundant, well preserved,  
361 fragile diatom frustules. This suggests that the apatite in core 25005 is authigenic and represents a

362 site of very recent phosphogenesis, likely Holocene in age. The lack of obvious giant sulfide-  
363 oxidizing bacteria at the site, however, makes it possible that active phosphogenesis at this site  
364 ceased, perhaps because the area of most intense upwelling and biomass accumulation had  
365 shifted northwards (Compton & Bergh, 2016).

366 Diagenetic pyrite first appears within the apatite maxima zone and increases downward in  
367 core 25005. This suggests the establishment of sulfidic conditions and a sharp redoxcline in the  
368 shallow subsurface (Figures 3d–e). Such diagenetic conditions are consistent with microbial  
369 redox-driven polyphosphate cycling, which invokes active and fluctuating redoxclines  
370 (Ruttenberg & Berner, 1993; Brock & Schulz-Vogt, 2011). A possible process which resulted in  
371 the apatite enrichment in core 25005 was proposed by Schulz & Schulz (2005), based on a study  
372 of the diatomaceous mudbelt to the north of the cores studied here. They found that the peak of  
373 sulfur-oxidizing *Thiomargarita* abundance coincided with peak dissolved and solid-phase  
374 phosphate concentration in the sediments, suggesting that phosphate pumping by these organisms  
375 leads to supersaturation with respect to apatite precursors, as the subsurface environment  
376 fluctuates between suboxic and sulfidic.

377 The apatitic pellets in the studied cores are ubiquitously composed of agglutinated,  
378 micron-sized, rod-shaped apatite particles that have coalesced into larger aggregates. They show  
379 recrystallization and growth from simple rod-shaped particles to dumbbell-shaped, and finally  
380 spherical particles (Figures 6, 9). Sequential recrystallization of apatite in the pellets is well  
381 illustrated by XRD and electron diffraction characteristics of apatite in the studied cores. They  
382 reveal a noticeably lower crystallinity and highly variable unit cell values of the authigenic *in situ*  
383 apatite in core 25005 in comparison with the redeposited apatite in the core GC4 (Figure 3b).

384 Similarly, the inner layers of the concentric rod-shaped particles show greater crystallinity  
385 compared to those in outer layers (Figure 7i–j).

386 Earlier studies of poorly consolidated phosphatic concretions in the Namibian  
387 diatomaceous mud (Baturin, 2000; Compton & Bergh, 2016) have suggested that the concretions  
388 initially formed as replacements of carbonaceous shells or infillings of sediment pore space  
389 (Compton & Bergh, 2016), possibly via localized and rapid apatite nucleation events triggered by  
390 phosphate-accumulating bacteria (Krajewski *et al.*, 1994; Schulz & Schulz, 2005). Our data  
391 indicate that sedimentary authigenic apatite is nucleated as ellipsoidal, 50–200 nm-sized electron  
392 dense areas. Growth of the rod-shaped particles then proceeds concentrically by addition of  
393 layers composed of nanocrystalline apatite. It appears that rod-shaped apatite particles are  
394 nucleated simultaneously at numerous sites within sediment pore water, and that apatite growth  
395 on individual particles proceeds episodically at different rates. The electron-dense layers in the  
396 concentric rod-shaped particles are composed of tightly packed, minute apatite crystallites that  
397 possibly represent periods of higher supersaturation (Figure 7b). Higher levels of apatite  
398 supersaturation – meaning the extent to which solute concentration exceeds thermodynamically  
399 determined solubility – result in higher rates of apatite precursor precipitation, as increasing  
400 supersaturation make the precipitation less dependent on distinct nucleation templates and allow  
401 for the precipitation of more soluble precursor phases (Krajewski *et al.*, 1994). By contrast, the  
402 porous layers are composed of crystallites tens of nm in size and could represent the growth of  
403 rod-shaped particles at lower supersaturation levels (Figures 7). Up to 12 alternating concentric  
404 layers were found in rod-shaped particles, and typically the electron-dense layers are wider  
405 compared to porous layers (Figure 7b). The outer layers of the rod-shaped particles appear wider,

406 possibly due to a geometric effect of the cross-sections cutting through the ellipsoidal rod-shaped  
407 particles at different distances with respect to their center (*e.g.*, Cosmidis *et al.*, 2013). Similar  
408 nanometer scale autocatalytic self-organization of the precipitates, due to oscillations in the local  
409 microenvironment, is known in silica-carbonate biomorphs (*e.g.*, Nakouzi *et al.*, 2015), and can  
410 result in formation of intrinsic mineralized banding patterns with the same periodicity (Montalti  
411 *et al.*, 2017). Therefore, such layering observed in rod-shaped apatite particles could be the result  
412 of alternating levels of phosphate input, in turn, a result of intermittent microbial phosphate  
413 pumping by polyphosphate-accumulating bacteria (Schulz & Schulz, 2005; Jones *et al.*, 2016).  
414 Alternatively, the pattern might be similar to Liesegang banding, in which case the formation of  
415 layers could arise from a supersaturation-nucleation-depletion cycle, or by post-nucleation  
416 Ostwald-ripening type processes, without requiring a fluctuating phosphate input (Nakouzi &  
417 Steinbock, 2016). However, the thinnest Liesegang bands observed in natural and experimental  
418 settings are on the order of a few to 100  $\mu\text{m}$  thick (*e.g.*, Bensemann *et al.*, 2005), much larger  
419 than the bands observed in our study.

420 We interpret the concentric rod-shaped particles to be primary phosphatic nuclei, possibly  
421 growing episodically at the fluctuating (sub)oxic-sulfidic redoxcline. There is no evidence of a  
422 visible substrate for heterogeneous nucleation inside the rod-shaped particles, except for perhaps  
423 the organic matter closely associated with the apatite particles. Instead, the high number of rod-  
424 shaped particles ( $>10^9$  particles per  $\text{cm}^3$ ) seems to be more consistent with homogeneous  
425 nucleation from a highly supersaturated solution with dissolved phosphate concentration  $>400$   
426  $\mu\text{M}$  (*e.g.*, above the threshold for the nucleation of low interfacial-energy apatite precursor  
427 phases), as has been previously suggested for other phosphorites (Krajewski *et al.*, 1994). Such

428 high dissolved phosphate levels might be the result of phosphate pumping by polyphosphate-  
429 accumulating bacteria (Schulz & Schulz, 2005), which may or may not be giant sulfur bacteria  
430 (Jones et al., 2016). It is particularly interesting that the density of apatite nuclei in Namibian  
431 apatitic pellets is in the same range as in other recent and ancient phosphorites (Lamboy, 1990a),  
432 possibly suggesting a universal mechanism behind authigenic apatite precipitation in  
433 phosphogenic environments.

434           It has been shown that sedimentary authigenic apatite precipitation involves different  
435 metastable fluoride-poor (semi-)amorphous Ca-phosphate precursor phases, such as struvite,  
436 octacalcium phosphate or amorphous calcium(-magnesium) phosphate. These phases are  
437 subsequently converted into carbonate fluorapatite – the most thermodynamically-stable apatite  
438 phase in seawater (Jahnke, 1984; Knudsen & Gunter, 2002) – through a dissolution-re-  
439 precipitation process or alternatively directly through solid-phase transitions (Froelich *et al.*,  
440 1988; Krajewski *et al.*, 1994; Baturin, 2000; Arning *et al.*, 2009b). The absence of amorphous  
441 precursor phases in analyzed samples is consistent with termination of apatite precipitation at the  
442 studied sites some time ago. Nonetheless, since the critical role of amorphous precursors in  
443 apatite precipitation has been confirmed in both laboratory experiments and in marine settings  
444 (van Cappellen & Berner, 1991; Krajewski *et al.*, 1994; Schenau *et al.*, 2000; Golubev et al.,  
445 1999; Gunnars *et al.*, 2004; Borkiewicz *et al.*, 2010; Oxmann & Schwendenmann, 2014), we  
446 expect these phases must have precipitated first. Changing structural ordering of the Ca-  
447 phosphate phase is also suggested by TEM diffraction of the less-matured apatite on the rims of  
448 the apatite particles that does show some smearing – a sign of misorientation of individual  
449 nanocrystallites, which is a characteristic of mosaic crystals derived from amorphous precursors

450 (Figure 7j). Furthermore, the lath-shaped (well crystallized) crystallites nucleating at the rod-  
451 shaped particles and forming larger intersecting dumbbell-to-spherical particles might result from  
452 thermodynamically driven recrystallization of nanocrystalline primary apatite involving Ostwald  
453 ripening type processes (*e.g.*, Voorhees; 1985) that are suggested as a mechanism in the  
454 formation of Liesegang banding (*e.g.*, Kai *et al.*, 1982). The less-well defined apatite matrix  
455 might represent the end product of the intergrowth and re-crystallization of primary rod-shaped  
456 apatite particles, or could alternatively be a more direct result of the dehydration and  
457 recrystallization of amorphous Ca-phosphate mass (Baturin, 2000).

458           The growth of very similar rod, dumbbell and spherical-shaped apatite particles has been  
459 previously reported in laboratory experiments conducted at high supersaturation levels  
460 (Krajewski *et al.*, 1994; Ruan *et al.*, 2013). An important aspect in understanding the genesis of  
461 such apatite microstructures is the occurrence of different types of microstructures forming a  
462 sequence of evolving morphologies – from rod-shaped particles with bulged distal ends to  
463 dumbbells and semi-spherical particles (Figure 9). A similar assemblage of microstructures  
464 termed “fluorapatite-gelatin nanocomposites” has been reported to occur in double-diffusion  
465 experiments using a variety of organic substrata (Kniep & Busch, 1996; Busch *et al.*, 1999;  
466 Kniep & Simon, 2006; Wu *et al.*, 2010). In double-diffusion experiments investigating the  
467 influence of organic materials on the precipitation of apatite, numerous morphologies evolved  
468 from prismatic to dumbbell-like to spherical amongst the precipitates that nucleated and grew  
469 within a polymeric gelatin gel (Crosby & Bailey, 2017; 2018; Figure 10). Interestingly, many  
470 have a distinctly biological appearance despite being abiological, and they resemble features  
471 described in the Namibian phosphate pellets. Such a form of fractal-like reorientation of crystal

472 growth has been found to be controlled by an intrinsic dipolic field generated by organic  
473 macromolecules that are incorporated in the nanostructure of the particles (Simon *et al.*, 2006). A  
474 very similar form of crystal growth is interpreted to have formed the succession of rod-shaped to  
475 dumbbell to spherical/radial microstructures found on the Namibian shelf, although Baturin and  
476 Titov (2006) have alternatively explained the formation of spherical particles through the  
477 dehydration and recrystallization of amorphous Ca-phosphate gels.

478           The lab-grown nanocomposites possess a distinctive inner structure – crystallites  
479 emanating from the core mostly grow parallel to the long axis, but tend to start to orient at an  
480 angle as the composites grow (Brickmann *et al.*, 2010). The slightly angled orientation of the  
481 crystallites in the Namibian rod-shaped particles is evident in apatitic pellets in both cores  
482 (Figures 6c–d, 7). In Namibian phosphorites, the growth of the recrystallized apatite particles  
483 composed of radiating lath-shaped crystallites is seeded on concentric rod-shaped particles.  
484 Similar to the lab-grown nanocomposites (Figure 10a–b), most of the subsequent growth is  
485 concentrated at the distal ends of the rod-shaped particles and directed outward (Figure 7c). This  
486 results in bulging of the distal ends of the particles (Figure 9b–c), where cross-sections reveal that  
487 the growth layers are widest at the distal ends of the rod-shaped particles (Figure 7b). It further  
488 leads to the formation of radial/spherical particles that compose most of the volume of the  
489 macroscopic apatitic pellets (Figure 9d, 10c). In addition, besides the very similar morphology,  
490 the rod-shaped particles commonly appear in association with substrata composed of organic  
491 macromolecules (Figure 6). The latter likely serve as nucleation surfaces for the formation of the  
492 fluorapatite-gelatin nanocomposites and may also induce the distal reorientation of crystal growth  
493 as noted by Simon *et al.* (2006). This also suggests that the pellets form by aggregation of

494 recrystallizing rod-shaped apatite particles, and that there is not much outward growth of the  
495 primary apatitic pellets themselves. However, concentric rims on reworked/matured pellets in  
496 GC4 core (Figure 5a, similar to 10f) possibly indicate that Ca-phosphate precipitation has been  
497 repeatedly renewed using the surface of the preexisting pellet as the nucleation template.

498

### 499 **The role of biological templates in apatite nucleation and growth**

500 The pervasive rod-shaped apatite particles in Namibian apatitic pellets bear a strong superficial  
501 resemblance to microbial casts due to their generally similar sizes, and co-occurrence with  
502 organic substance that may have once represented microbial EPS (Figure 6). Very similar fabrics  
503 have been found in various phosphorites that were previously interpreted as aggregations of  
504 microbial casts (Lambooy, 1990a; Zanin & Zamirailova, 2011). Their formation was hypothesized  
505 to be the result of nucleation of apatite nanocrystals on microbial cell walls, which are known to  
506 provide suitable binding sites for biologically induced phosphate mineral formation (Konhauser  
507 *et al.*, 1994). The minerals encrusting the microbes then start to grow and coalesce, until the  
508 organic structures are wholly replaced by apatite (*e.g.*, Lepland *et al.*, 2014). Indeed, the fast-  
509 growing field of biomineralization research has provided a myriad of experimental evidence to  
510 support the importance of microbes in both providing nucleation surfaces and exerting more or  
511 less direct control over the precipitation of minerals via extra- or intracellular enzymes, the  
512 concentration of ions, or the excretion of EPS material (Konhauser & Riding, 2012). Specifically,  
513 functional groups on cell walls and/or polymeric strands of EPS provide suitable binding sites for  
514 calcium cations and have thus been shown to promote the nucleation of calcium carbonate



515 minerals (Benzerara *et al.*, 2004), although the importance of such surfaces on apatite  
516 precipitation decreases with higher degrees of supersaturation and higher precipitation rates  
517 (Krajewski *et al.*, 1994).

518         Despite many microbes having developed mechanisms to prevent becoming encrusted in  
519 authigenic minerals (Schultze-Lam *et al.*, 1992; Phoenix and Konhauser, 2008; Hegler *et al.*,  
520 2010), phosphatization is a well-known means by which microbes and metazoans can be  
521 preserved as fossils (Crosby & Bailey, 2012). The rapid formation of sedimentary authigenic  
522 apatite leads to the phosphatization of widely different biological structures, including nanoscale  
523 fibrous organic structures in linguliform brachiopods (Lang *et al.*, 2016), fungal mats (Br  h  ret,  
524 1991), filamentous cyanobacteria mats and stromatolites (Rao *et al.*, 2000), filamentous sulfur  
525 bacteria (Bailey *et al.*, 2013), and other bacterial forms (Krajewski *et al.*, 1994). In microbial  
526 structures the mechanism remains the same in most cases – extracellular precipitation of apatite,  
527 which tends to produce external molds of microbes. Conspicuous microbial structures have also  
528 been found in a wide variety of ancient phosphorites (Krajewski *et al.*, 1994; Crosby & Bailey,  
529 2012; Bailey *et al.*, 2013; Cosmidis *et al.*, 2013), up to and including, some of the earliest  
530 significant phosphorites in the world, e.g., the 1.7 Ga Jhamarkotra Formation, India (Crosby *et*  
531 *al.*, 2014), 1.85 Ga Michigamme Formation, USA (Hiatt *et al.*, 2015), 1.88 Ga Ferriman Group,  
532 India (Edwards *et al.*, 2012), and ~2 Ga Zaonega Formation, Russia (Lepland *et al.*, 2014). The  
533 very common occurrence of phosphatized microbial cells in phosphatic sediments has been  
534 interpreted as evidence of the direct role of microbial surfaces in the nucleation of phosphate  
535 minerals (Lamboy, 1990a), the role of microbes in concentrating ions in pore waters (Schulz &

536 Schulz, 2005; Goldhammer *et al.*, 2010), or simply as a consequence of the rapid precipitation of  
537 authigenic apatite, which tends to indiscriminately phosphatize surfaces (Krajewski *et al.*, 1994).

538 A controversial class of phosphatic microstructures are the densely-packed aggregates of  
539 small rod-shaped particles marked by rounded, non-crystalline appearance and a length of a few  
540  $\mu\text{m}$ , which have been reported from a variety of recent and ancient phosphorites (Bremner, 1980;  
541 O'Brien *et al.*, 1981; Mullins & Rasch, 1985; Bersenev *et al.*, 1986; Garrison *et al.*, 1987; Rao &  
542 Nair, 1988; Garrison & Kastner, 1990; Lewy, 1990; Lamboy, 1993, 1994; Baturin, 2000). Their  
543 overall resemblance to phosphatized microbial mats has led many researchers to interpret them as  
544 phosphatized casts of rod-shaped bacteria (O'Brien *et al.*, 1981; Lamboy, 1990a, 1990b;  
545 Br  h  ret, 1991; Zanin & Zamirailova, 2011).

546 A large body of laboratory work has also been conducted on the precipitation of apatite in  
547 the field of biomaterials research, motivated by the goal of understanding biomineralization of  
548 human bone and teeth, and by possible medical applications, such as re-growing bone tissue  
549 (Vallet-Reg   & Gonz  lez-Calbet, 2004). Since controlled biomineralization in vertebrates takes  
550 place in a complex environment of organic scaffolds and catalysts, the research has focused on  
551 the effects of polymers as nucleation templates or additives, while also keeping in mind the effect  
552 of inorganic additives, pH and temperature (Bleek & Taubert, 2013). These studies have shown  
553 an exceedingly diverse picture of the possible apatite mineral forms capable of growing under a  
554 large variety of synthesis conditions (Lin *et al.*, 2014). Densely-packed, rod-shaped particles are  
555 often described forming in such experiments (*e.g.* Ruan *et al.*, 2013), and similarly to what is  
556 found in Namibian phosphorites, some of this work shows that rod-shaped particles transform  
557 into dumbbell-shaped and radial-spherical particles in the presence of organic macromolecules.

558 These structures are equally common in calcite, dolomite, and Fe-oxyhydroxide precipitates  
559 formed in the presence of organic substances (Meldrum & Hyde, 2001; van Lith *et al.*, 2003;  
560 Meldrum & Cölfen, 2008; Tourney & Ngwenya, 2014).

561 Krajewski *et al.* (1994), along with other researchers, expressed a skepticism of all  
562 putative bacterial forms in phosphorites (except filamentous cyanobacteria and fungi) and  
563 suggested that only morphologies which have been demonstrated to form during experimental  
564 mineralization of microbes can be considered as potential microbial fossils. Such forms are  
565 mainly empty or partially infilled coccoid to rod-shapes, in essence, forms that contain a hollow  
566 lumen (Cosmidis *et al.*, 2013). Microscopic rod-shaped particles in the Namibian phosphorites  
567 reported here, and in previous studies (Baturin, 2002; Baturin & Titov, 2006; Titov & Baturin,  
568 2008; Compton & Bergh, 2016), bear significant resemblance to phosphatized microbial remains.  
569 These appear as rod-shaped dubiofossils with somewhat consistent sizes, attached to pore walls  
570 in a microbially active sedimentary environment, surrounded by organic macromolecular  
571 structures that possibly represent dessicated EPS (*e.g.*, compare Figure 6b with Figure 7 in  
572 Nealson, 1997). There are, however, significant problems with this interpretation, as has  
573 previously been pointed out regarding the Namibian phosphorites by Baturin and Titov (2006)  
574 and Titov and Baturin (2008). For instance, the nanostructure of the rod-shaped particles, as  
575 imaged via TEM in this study, indicate that the particles are not phosphatized microbes (Figure  
576 7). A microbe would first be encrusted on the outside, with mineralization reaching the inside of  
577 the cell after it has lysed (Konhauser *et al.*, 1994). This would, ideally, result in distinct rim and  
578 core structures, representing the different stages of mineralization (*e.g.*, Lepland *et al.*, 2014).  
579 The innermost layer of the rod-shaped particles could be construed as a mineralized microbe, if

580 not for its small size – a diameter of <200 nm is much less than that generally attributed for  
581 viable non-parasitic bacteria (Luef *et al.*, 2015). Secondly, a significant number of the rod-shaped  
582 particles show intersecting/intertwining with respect to one another and/or a common point of  
583 origin that is not characteristic of microbial casts (Figures 8a–b). Although this may be the result  
584 of post-nucleation growth of what were originally much smaller and non-intersecting apatite  
585 particles, in most cases, this appears to be a primary feature possessed by even the innermost  
586 layers of the rod-shaped particles, as evident in TEM-micrographs (Figure 7b).

587         The question then becomes how did the apatite precursor phases nucleate, and which, if  
588 any nucleation templates were involved. On the one hand, the nanoscale structure of the rod-  
589 shaped apatite particles does not incorporate any other mineral components. On the other hand,  
590 several lines of evidence point to the role of organic matter in apatite nucleation: (i) the apatite  
591 particles commonly appear (almost without exception) in association with organic substances  
592 (Figure 6); (ii) the microstructures that form most of the apatite matrix are similar to laboratory  
593 fluorapatite-gelatin nanocomposite precipitates, in which organic macromolecules are intimately  
594 tied to apatite nanostructure and play a key role in controlling apatite growth (Kniep & Simon,  
595 2006; Simon *et al.*, 2006); (iii) the occurrence of porous layers within the rod-shaped apatite  
596 particles that are enriched in carbon and sulfur, likely proxies for organic matter (Figure 7d–f).  
597 Accepting the identification of the apatite microstructures in Namibian phosphorites as analogous  
598 to fluorapatite-gelatin nanocomposites, the crystal growth and formation of this specific  
599 morphology seems to be controlled by organic macromolecules of a certain type (*e.g.*, Simon *et*  
600 *al.*, 2006).

601           While characterizing the exact nature of this organic substance is beyond the scope of the  
602 present study, we can hypothesize that in the Namibian shelf sediments, these substances most  
603 likely derive from microbial cell walls, the products of microbial breakdown of sedimentary  
604 organic matter, or relicts of bacterially excreted EPS. It is then possible that organic polymeric  
605 macromolecules, for example those that comprise the organic portion of EPS, served as the  
606 primary nucleation environment during the formation of rod-shaped particles and its precursor  
607 phases. EPS is known to provide a template for adsorption of metal cations to which anions are  
608 attracted, thus inducing local mineral supersaturation (Tourney & Ngwenya, 2014).

609           Although the abundant rod-shaped particles in Namibian apatitic pellets are not fossilized  
610 microbes, the authigenic precipitation of apatite can be seen as having been largely controlled by  
611 microbially-produced processes (e.g., phosphate pumping) and substances (e.g., EPS or other  
612 microbially-produced organic substances). Since the association of phosphatic facies and strata  
613 with organic matter is widely recognized in the geologic record (Krajewski *et al.*, 1994), it may  
614 well be that nucleation of calcium phosphate minerals on organic nucleation substrata played  
615 similar roles in the formation of authigenic apatite in other recent and ancient phosphorite  
616 deposits.

617

## 618 **Conclusions**

619 Microbial influences on sedimentary authigenic apatite precipitation from an area known for  
620 modern phosphogenesis were studied. Phosphorus in these sediments is mainly present as sub-  
621 mm apatitic pellets, which are, in turn, mainly composed of intergrown ~1 µm long, rod-shaped

622 apatite particles that co-occur with organic substance. The dense distribution ( $>10^9$  per  $\text{cm}^3$ ), a  
623 lack of visible nucleation templates in the nanostructure, and distinctive growth patterns  
624 incorporating organic matter, indicate that the phosphate minerals in the P-rich sediments on the  
625 Namibian shelf may have nucleated on organic substrata, such as polymeric strands of EPS, in  
626 pore waters supersaturated with respect to an apatite precursor. Furthermore, as similar structures  
627 are common in other phosphorites, this potentially represents a general mechanism for the  
628 precipitation of P-rich sediments.

629           The apatite microstructures range from rod-shaped to bulged forms, dumbbells and  
630 spherical particles, representing a growth continuum very similar to previously reported lab-  
631 grown apatite structures in highly-supersaturated solutions in organic matrices – “fluorapatite-  
632 gelatin nanocomposites” or phosphatic objects precipitated in the gelatin matrix of a double  
633 diffusion gradient apparatus. Considering the similar inner structures of the lab grown  
634 microstructures to the apatite structures in the Namibian phosphorites, one can infer that the  
635 environmental precipitates formed through a mechanism analogous to that of the lab-grown  
636 nanocomposites.

637           The closely intertwined organic matrix in the nanostructure of the apatite is most likely a  
638 byproduct of microbially-produced organic matter and might act as a major nucleation template  
639 for the apatite precursor phases. This could provide a further indirect microbial control on the  
640 formation of phosphorites. However, the superficial resemblance of such rod-shaped apatite  
641 particles to microbial casts, as has been previously suggested, is not borne out under closer  
642 scrutiny, urging caution when looking for microfossils in similar material.

643

## 644 **Acknowledgments**

645 The authors would like to thank the organizers and participants of the Regional Graduate  
646 Network in Oceanography Discovery Camp 2015 that is funded by the Agouron Institute and the  
647 Scientific Committee for Oceanographic Research (SCOR); the crew of R/V *Mirabilis* and the  
648 University of Namibia for access to coring sites and help with sample gathering; Nathan Gerein  
649 for SEM work in the University of Alberta; Liisa Lang for help with TEM analyses; and Leslie J.  
650 Robbins for helpful comments. Three anonymous reviewers are thanked for constructive  
651 comments and insights that have greatly improved the manuscript. This study was supported by  
652 the Ministry of Education and Research of Estonia mobility grant within Archimedes  
653 Foundation's The Kristjan Jaak Scholarship program "Doctoral Study Abroad" to KM; Estonian  
654 Science Agency under grant PUT696 to KK; Natural Sciences and Engineering Research Council  
655 of Canada Discovery grant RGPIN-165831 to KOK, and by a grant from the U.S. National  
656 Science Foundation EAR-1057119 to JVB.

657

## 658 **References**

659 Arning, E. T., Birgel, D., Brunner, B., & Peckmann, J. (2009a). Bacterial formation of phosphatic  
660 laminites off Peru. *Geobiology*, 7, 295–307.

661 Arning, E. T., Birgel, D., Schulz-Vogt, H. N., Holmkvist, L., Jørgensen, B. B., Larson, A., &  
662 Peckmann, J. (2008). Lipid biomarker patterns of phosphogenic sediments from upwelling  
663 regions. *Geomicrobiology Journal*, *25*, 69–82.

664 Arning, E. T., Lückge, A., Breuer, C., Gussone, N., Birgel, D., & Peckmann, J. (2009b). Genesis  
665 of phosphorite crusts off Peru. *Marine Geology*, *262*, 68–81.

666 Bailey, J. V., Corsetti, F. A., Greene, S. E., Crosby, C. H., Liu, P., & Orphan, V. J. (2013.)  
667 Filamentous sulfur bacteria preserved in modern and ancient phosphatic sediments: Implications  
668 for the role of oxygen and bacteria in phosphogenesis. *Geobiology*, *11*, 397–405.

669 Baturin, G. N. (2000). Formation and evolution of phosphorite grains and nodules on the  
670 Namibian Shelf from Recent to Pleistocene. In C. R. Glenn, L. Prevot-Lucas, & J. Lucas (Eds.),  
671 *Marine Authigenesis: From Global to Microbial*, *SEPM Special Publication*, vol. 66 (pp. 185–  
672 200). Tulsa, OK: SEPM Society for Sedimentary Geology.

673 Baturin, G. N. (2002). Nodular fraction of phosphatic sand from the Namibia Shelf. *Lithology*  
674 *and Mineral Resources*, *37*, 1–17.

675 Baturin, G. N., & Bezrukov, P. L. (1979). Phosphorites on the sea floor and their origin. *Marine*  
676 *Geology*, *31*, 317–332.

677 Baturin, G. N., & Titov, A. T. (2006). Biomorphic formations in recent phosphorites.  
678 *Oceanology*, *46*, 711–715.

679 Bensemann, I. T., Fialkowski, M., & Grzybowski, B. A. (2005). Wet stamping of microscale  
680 periodic precipitation patterns. *The Journal of Physical Chemistry B*, *109*, 2774–2778.



681 Benzerara, K., Menguy, N., Guyot, F., Skouri, F., de Luca, G., Barakat, M., & Heulin, T. (2004).  
682 Biologically controlled precipitation of calcium phosphate by *Ramlibacter tataouinensis*. *Earth*  
683 *and Planetary Science Letters*, *228*, 439–449.

684 Bersenev, I., Baturin, G., Lelikov, E., & Gusev, V. (1986). Neogene phosphorites of the Sea of  
685 Japan. In W. C. Burnett, & S. R. Riggs (Eds.), *Phosphate Deposits of the World: Volume 3,*  
686 *Neogene to Modern Phosphorites* (pp. 167–176). Cambridge, UK: Cambridge University Press.

687 Bintanja, R., van de Wal, R. S. W., & Oerlemans, J. (2005). Modelled atmospheric temperatures  
688 and global sea levels over the past million years. *Nature*, *437*, 125–128.

689 Bleek, K., & Taubert, A. (2013). New developments in polymer-controlled, bioinspired calcium  
690 phosphate mineralization from aqueous solution. *Acta Biomaterialia*, *9*, 6283–6321.

691 Borkiewicz, O., Rakovan, J., & Cahill, C. L. (2010). Time-resolved in situ studies of apatite  
692 formation in aqueous solutions. *American Mineralogist*, *95*, 1224–1236.

693 Bréhéret, J.-G. (1991). Phosphatic concretions in black facies of the Aptian-Albian Marnes  
694 bleues Formation of the Vocontian basin (SE France), and at site DSDP 369: Evidence of benthic  
695 microbial activity. *Cretaceous Research*, *12*, 411–435.

696 Bremner, J.M. (1980). Concretionary phosphorite from SW Africa. *Journal of the Geological*  
697 *Society*, *137*, 773–786.

698 Brickmann, J., Papparcone, R., Kokolakis, S., Zahn, D., Duchstein, P., Carrillo-Cabrera, W.,  
699 Simon, P., & Kniep, R. (2010). Fluorapatite-gelatine nanocomposite superstructures: New  
700 insights into a biomimetic system of high complexity. *ChemPhysChem*, *11*, 1851–1853.

701 Brock, J., & Schulz-Vogt, H. N. (2011). Sulfide induces phosphate release from polyphosphate in  
702 cultures of a marine Beggiatoa strain. *The ISME journal*, 5, 497–506.

703 Brown, W. E., Mathew, M., & Chow, L. C. (1984). Roles of octacalcium phosphate in surface  
704 chemistry of apatites. In D. N. Misra (Eds.), *Adsorption on and Surface Chemistry of*  
705 *Hydroxyapatite* (pp. 13–28). New York, NY: Plenum Press.

706 Brüchert, V., Currie, B., Peard, K. R., Lass, U., Endler, R., Dübecke, A., Julies, E., Leipe, T., &  
707 Zitzmann, S. (2006). Biogeochemical and physical control on shelf anoxia and water column  
708 hydrogen sulphide in the Benguela coastal upwelling system off Namibia. In L. Neretin (Eds.),  
709 *Past and Present Water Column Anoxia. Nato Science Series: IV: Earth and Environmental*  
710 *Sciences, vol 64* (pp. 161–193). New York, NY: Springer, Dordrecht.

711 Burnett, W. C. (1977). Geochemistry and origin of phosphorite deposits from off Peru and Chile.  
712 *Geological Society of America Bulletin*, 88, 813–823.

713 Burnett, W. C., Glenn, C. R., Yeh, C. C., Schultz, M., Chanton, J., & Kashgarian, M. (2000). U-  
714 series, 14C, and stable isotope studies of recent phosphatic “protocrusts” from the Peru margin.  
715 In C. R. Glenn, L. Prevot-Lucas, & J. Lucas (Eds.), *Marine Authigenesis: From Global to*  
716 *Microbial, SEPM Special Publication, vol. 66* (pp. 163–183). Tulsa, OK: SEPM Society for  
717 Sedimentary Geology.

718 Busch, S., Dolhaine, H., DuChesne, A., Heinz, S., Hochrein, O., Laeri, F., Podebrad, O., Vietze,  
719 U., Weiland, T., & Kniep, R. (1999). Biomimetic morphogenesis of fluorapatite-gelatin  
720 composites: Fractal growth, the question of intrinsic electric fields, core/shell assemblies, hollow

721 spheres and reorganization of denatured collagen. *European Journal of Inorganic Chemistry*,  
722 1999, 1643–1653.

723 Cappellen, P. van, & Berner, R. A. (1991). Fluorapatite crystal growth from modified seawater  
724 solutions. *Geochimica et Cosmochimica Acta*, 55, 1219–1234.

725 Carr, M.-E. (2001). Estimation of potential productivity in Eastern Boundary Currents using  
726 remote sensing. *Deep Sea Research Part II: Topical Studies in Oceanography*, 49, 59–80.

727 Compton, J. S., & Bergh, E. W. (2016). Phosphorite deposits on the Namibian shelf. *Marine*  
728 *Geology*, 380, 290–314.

729 Compton, J. S., Mulabisana, J., & McMillan, I. K. (2002). Origin and age of phosphorite from the  
730 Last Glacial Maximum to Holocene transgressive succession off the Orange River, South Africa.  
731 *Marine Geology*, 186, 243–261.

732 Compton, J. S., Wigley, R., & McMillan, I. K. (2004). Late Cenozoic phosphogenesis on the  
733 western shelf of South Africa in the vicinity of the Cape Canyon. *Marine Geology*, 206, 19–40.

734 Cordell, D., Drangert, J.-O., & White, S. (2009). The story of phosphorus: Global food security  
735 and food for thought. *Global Environmental Change, Traditional Peoples and Climate Change*,  
736 19, 292–305.

737 Cosmidis, J., Benzerara, K., Gheerbrant, E., Estève, I., Bouya, B., & Amaghazaz, M. (2013).  
738 Nanometer-scale characterization of exceptionally preserved bacterial fossils in Paleocene  
739 phosphorites from Ouled Abdoun (Morocco). *Geobiology*, 11, 139–153.

740 Crosby, C. H., & Bailey, J. V. (2012). The role of microbes in the formation of modern and  
741 ancient phosphatic mineral deposits. *Frontiers in Microbiology*, *3*, 241.

742 Crosby, C. H., & Bailey, J. V. (2017). Technical note: An economical apparatus for the  
743 observation and harvest of mineral precipitation experiments with light microscopy.  
744 *Biogeosciences*, *14*, 2151–2154.

745 Crosby, C. H., & Bailey, J. V. (2018). Experimental precipitation of apatite pseudofossils  
746 resembling fossil embryos. *Geobiology*, *16*, 80–87.

747 Crosby, C. H., Bailey, J. V., & Sharma, M. (2014). Fossil evidence of iron-oxidizing  
748 chemolithotrophy linked to phosphogenesis in the wake of the Great Oxidation Event. *Geology*,  
749 *42*, 1015–1018.

750 Dale, A. W., Bertics, V. J., Treude, T., Sommer, S., & Wallmann, K. (2013). Modeling benthic–  
751 pelagic nutrient exchange processes and porewater distributions in a seasonally hypoxic  
752 sediment: evidence for massive phosphate release by *Beggiatoa*? *Biogeosciences*, *10*, 629–651.

753 Delaney, M. L. (1998). Phosphorus accumulation in marine sediments and the oceanic  
754 phosphorus cycle. *Global Biogeochemical Cycles*, *12*, 563–572.

755 Eckardt, F. D., & Kuring, N. (2005). SeaWiFS identifies dust sources in the Namib Desert.  
756 *International Journal of Remote Sensing*, *26*, 4159–4167.

757 Edwards, C. T., Pufahl, P. K., Hiatt, E. E., & Kyser, T. K. (2012). Paleoenvironmental and  
758 taphonomic controls on the occurrence of Paleoproterozoic microbial communities in the 1.88 Ga  
759 Ferriman Group, Labrador Trough, Canada. *Precambrian Research*, *212–213*, 91–106.

760 Filippelli, G. M. (2011). Phosphate rock formation and marine phosphorus geochemistry: The  
761 deep time perspective. *Chemosphere*, *84*, 759–766.

762 Föllmi, K. B. (1996). The phosphorus cycle, phosphogenesis and marine phosphate-rich deposits.  
763 *Earth-Science Reviews*, *40*, 55–124.

764 Froelich, P. N., Arthur, M. A., Burnett, W. C., Deakin, M., Hensley, V., Jahnke, R., Kaul, L.,  
765 Kim, K.-H., Roe, K., Soutar, A., & Vathakanon, C. (1988). Early diagenesis of organic matter in  
766 Peru continental margin sediments: Phosphorite precipitation. *Marine Geology*, *80*, 309–343.

767 Garrison, R. E., & Kastner, M. (1990). Phosphatic sediments and rocks recovered from the Peru  
768 Margin during ODP Leg 112. *Proceedings of the Ocean Drilling Program, Scientific Results*,  
769 *112*, 111–134.

770 Garrison, R. E., Kastner, M., & Kolodny, Y. (1987). Phosphorites and phosphatic rocks in the  
771 Monterey Formation and related Miocene units, coastal California. In R. V. Ingersoll, W. G.  
772 Ernst (Eds.), *Cenozoic Basin Development of Coastal California*, vol. 6 (pp. 348–381).  
773 Englewood Cliffs, NJ: Prentice-Hall.

774 Goldhammer, T., Brüchert, V., Ferdelman, T. G., & Zabel, M. (2010). Microbial sequestration of  
775 phosphorus in anoxic upwelling sediments. *Nature Geoscience*, *3*, 557–561.

776 Goldhammer, T., Brunner, B., Bernasconi, S. M., Ferdelman, T. G., & Zabel, M. (2011).  
777 Phosphate oxygen isotopes: Insights into sedimentary phosphorus cycling from the Benguela  
778 upwelling system. *Geochimica et Cosmochimica Acta*, *75*, 3741–3756.

779 Golubev, S. V., Pokrovsky, O. S., & Savenko, V. S. (1999). Unseeded precipitation of calcium  
780 and magnesium phosphates from modified seawater solutions. *Journal of Crystal Growth*, *205*,  
781 354–360.

782 Gunnars, A., Blomqvist, S., & Martinsson, C. (2004). Inorganic formation of apatite in brackish  
783 seawater from the Baltic Sea: An experimental approach. *Marine Chemistry*, *91*, 15–26.

784 Hegler, F., Schmidt, C., Schwarz, H., & Kappler, A. (2010). Does a low-pH microenvironment  
785 around phototrophic FeII-oxidizing bacteria prevent cell encrustation by FeII minerals? *FEMS*  
786 *Microbiology Ecology*, *74*, 592–600.

787 Hiatt, E. E., Pufahl, P. K., & Edwards, C. T. (2015). Sedimentary phosphate and associated fossil  
788 bacteria in a Paleoproterozoic tidal flat in the 1.85Ga Michigamme Formation, Michigan, USA.  
789 *Sedimentary Geology*, *319*, 24–39.

790 Hirschler, A., Lucas, J., & Hubert, J.-C. (1990). Apatite genesis: A biologically induced or  
791 biologically controlled mineral formation process? *Geomicrobiology Journal*, *8*, 47–56.

792 Holmkvist, L., Arning, E. T., Küster-Heins, K., Vandieken, V., Peckmann, J., Zabel, M., &  
793 Jørgensen, B. B. (2010). Phosphate geochemistry, mineralization processes, and Thioploca  
794 distribution in shelf sediments off central Chile. *Marine Geology*, *277*, 61–72.

795 Inthorn, M., Mohrholz, V., & Zabel, M. (2006). Nepheloid layer distribution in the Benguela  
796 upwelling area off shore Namibia. *Deep Sea Research Part I: Oceanographic Research Papers*,  
797 *53*, 1423–1438.

798 Jahnke, R. A. (1984). The synthesis and solubility of carbonate fluorapatite. *American Journal of*  
799 *Science*, 284, 58–78.

800 Jahnke, R. A., Emerson, S. R., Roe, K. K., & Burnett, W. C. (1983). The present day formation  
801 of apatite in Mexican continental margin sediments. *Geochimica et Cosmochimica Acta*, 47, 259–  
802 266.

803 Jones, D. S., Flood, B. E., & Bailey, J. V. (2016). Metatranscriptomic insights into polyphosphate  
804 metabolism in marine sediments. *The ISME Journal*, 10, 1015–1019.

805 Kai, S., Müller, S. C., & Ross, J. (1982). Measurements of temporal and spatial sequences of  
806 events in periodic precipitation processes. *The Journal of Chemical Physics*, 76, 1392–1406.

807 Kniep, R., & Busch, S. (1996). Biomimetic growth and self-assembly of fluorapatite aggregates  
808 by diffusion into denatured collagen matrices. *Angewandte Chemie International Edition in*  
809 *English*, 35, 2624–2626.

810 Kniep, R., & Simon, P. (2006). Fluorapatite-gelatine-nanocomposites: Self-organized  
811 morphogenesis, real structure and relations to natural hard materials. In K. Naka (Ed.),  
812 *Biomineralization I, Topics in Current Chemistry*, vol. 270 (pp. 73–125). Berlin; Heidelberg:  
813 Springer.

814 Knudsen, A. C., & Gunter, M. E. (2002). Sedimentary phosphorites—an example: Phosphoria  
815 Formation, Southeastern Idaho, U.S.A. *Reviews in Mineralogy and Geochemistry*, 48, 363–389.

816 Konhauser, K. O., & Riding, R. (2012). Bacterial biomineralization. In A. H. Knoll, D. E.  
817 Canfield, & K. O. Konhauser (Eds.), *Fundamentals of Geobiology* (pp. 105–130). Chichester,  
818 UK: John Wiley & Sons.

819 Konhauser, K. O., Fyfe, W. S., Schultze-Lam, S., Ferris, F. G., & Beveridge, T. J. (1994). Iron  
820 phosphate precipitation by epilithic microbial biofilms in Arctic Canada. *Canadian Journal of*  
821 *Earth Sciences*, *31*, 1320–1324.

822 Krajewski, K. P., van Cappellen, P., Trichet, J., Kuhn, O., Lucas, J., Martin-Algarra, A., Prevot,  
823 L., Tewari, V. C., Gaspar, L., Knight, R. I., & Lamboy, M. (1994). Biological processes and  
824 apatite formation in sedimentary environments. *Eclogae Geologicae Helvetiae*, *87*, 701–745.

825 Lamboy, M. (1990a). Microstructures of a phosphatic crust from the Peruvian continental-margin  
826 - Phosphatised bacteria and associated phenomena. *Oceanologica Acta*, *13*, 439–451.

827 Lamboy, M. (1990b). Microbial mediation in phosphatogenesis: New data from the Cretaceous  
828 phosphatic chalks of northern France. *Geological Society, London, Special Publications*, *52*,  
829 157–167.

830 Lamboy, M. (1993). Phosphatization of calcium carbonate in phosphorites: microstructure and  
831 importance. *Sedimentology*, *40*, 53–62.

832 Lamboy, M. (1994). Nanostructure and genesis of phosphorites from ODP Leg 112, the Peru  
833 margin. *Marine Geology*, *118*, 5–22.



834 Lang, L., Kirsimäe, K., & Vahur, S. (2016.) Diagenetic fate of bioapatite in linguliform  
835 brachiopods: multiple apatite phases in shells of Cambrian lingulate brachiopod *Ungula ingraca*  
836 (Eichwald). *Lethaia*, *49*, 13–27.

837 Lepland, A., Joosu, L., Kirsimäe, K., Prave, A. R., Romashkin, A. E., Črne, A. E., Martin, A. P.,  
838 Fallick, A. E., Somelar, P., Üpraus, K., Mänd, K., Roberts, N. M. W., van Zuilen, M. A., Wirth,  
839 R., & Schreiber, A. (2014). Potential influence of sulphur bacteria on Palaeoproterozoic  
840 phosphogenesis. *Nature Geoscience*, *7*, 20–24.

841 Lewy, Z. (1990). Pebbly phosphate and granular phosphorite (Late Cretaceous, southern Israel)  
842 and their bearing on phosphatization processes. *Geological Society, London, Special*  
843 *Publications*, *52*, 169–178.

844 Lin, K., Wu, C., & Chang, J. (2014). Advances in synthesis of calcium phosphate crystals with  
845 controlled size and shape. *Acta Biomaterialia*, *10*, 4071–4102.

846 Lith, Y. van, Warthmann, R., Vasconcelos, C., & Mckenzie, J. A. (2003). Sulphate-reducing  
847 bacteria induce low-temperature Ca-dolomite and high Mg-calcite formation. *Geobiology*, *1*, 71–  
848 79.

849 Luef, B., Frischkorn, K. R., Wrighton, K. C., Holman, H.-Y. N., Birarda, G., Thomas, B. C.,  
850 Singh, A., Williams, K. H., Siegerist, C. E., Tringe, S. G., Downing, K. H., Comolli, L. R., &  
851 Banfield, J. F. (2015). Diverse uncultivated ultra-small bacterial cells in groundwater. *Nature*  
852 *Communications*, *6*, 6372.

853 Martens, C. S., & Harriss, R. C. (1970). Inhibition of apatite precipitation in the marine  
854 environment by magnesium ions. *Geochimica et Cosmochimica Acta*, *34*, 621–625.

855 Meldrum, F. C., & Cölfen, H. (2008). Controlling mineral morphologies and structures in  
856 biological and synthetic systems. *Chemical Reviews*, *108*, 4332–4432.

857 Meldrum, F. C., & Hyde, S. T. (2001). Morphological influence of magnesium and organic  
858 additives on the precipitation of calcite. *Journal of Crystal Growth*, *231*, 544–558.

859 Midgley, J. (2012). Sandpiper project. Proposed recovery of phosphate enriched sediments from  
860 the marine mining licence area no. 170 off Walvis Bay Namibia. Environmental impact  
861 assessment report for the marine component. Final report. J. Midgley & Associates.  
862 [http://www.envirod.com/draft\\_environmental\\_impact\\_report2.html](http://www.envirod.com/draft_environmental_impact_report2.html). Accessed 22 Dec 2017.

863 Montalti, M., Zhang, G., Genovese, D., Morales, J., Kellermeier, M., & García-Ruiz, J. M.  
864 (2017). Local pH oscillations witness autocatalytic self-organization of biomorphic  
865 nanostructures. *Nature Communications*, *8*, ncomms14427.

866 Mullins, H. T., & Rasch, R. F. (1985). Sea-floor phosphorites along the Central California  
867 continental margin. *Economic Geology*, *80*, 696–715.

868 Nakouzi, E., Ghossoub, Y. E., Knoll, P., & Steinbock, O. (2015). Biomorph oscillations self-  
869 organize micrometer-scale patterns and nanorod alignment waves. *The Journal of Physical*  
870 *Chemistry C*, *119*, 15749–15754.

871 Nakouzi, E., & Steinbock, O. (2016). Self-organization in precipitation reactions far from the  
872 equilibrium. *Science Advances*, *2*, e1601144.

873 Neelson, K. H. (1997). Sediment bacteria: Who's there, what are they doing, and what's new?  
874 *Annual Review of Earth and Planetary Sciences*, 25, 403–434.

875 Nemliher, J. (1999). Mineralogy of Phanerozoic skeletal and sedimentary apatites: An XRD  
876 study. *Dissertationes Geologicae Universitatis Tartuensis*, 135 pp. Tartu, Estonia: Tartu  
877 University Press.

878 Noffke, A., Hensen, C., Sommer, S., Scholz, F., Bohlen, L., Mosch, T., Graco, M., & Wallmann,  
879 K. (2012). Benthic iron and phosphorus fluxes across the Peruvian oxygen minimum zone.  
880 *Limnology and Oceanography*, 57, 851–867.

881 O'Brien, G., & Heggie, D. (1988). East Australian continental margin phosphorites. *Eos*,  
882 *Transactions of the American Geophysical Union*, 69, 2.

883 O'Brien, G. W., Harris, J. R., Milnes, A. R., & Veeh, H. H. (1981). Bacterial origin of East  
884 Australian continental margin phosphorites. *Nature*, 294, 442–444.

885 O'Brien, G. W., & Veeh, H. H. (1980). Holocene phosphorite on the East Australian continental  
886 margin. *Nature*, 288, 690–692.

887 Oxmann, J. F., & Schwendenmann, L. (2014). Quantification of octacalcium phosphate,  
888 authigenic apatite and detrital apatite in coastal sediments using differential dissolution and  
889 standard addition. *Ocean Science*, 10, 571–585.

890 Phoenix, V. R., & Konhauser, K.O. (2008). Benefits of bacterial biomineralization. *Geobiology*,  
891 6, 303–308.

- 892 Rao, V. P., & Nair, R. R. (1988). Microbial origin of the phosphorites of the western continental  
893 shelf of India. *Marine Geology*, *84*, 105–110.
- 894 Rao, V. P., Rao, K. M., & Raju, D. S. N. (2000). Quaternary phosphorites from the continental  
895 margin off Chennai, Southeast India: Analogs of ancient phosphate stromatolites. *Journal of*  
896 *Sedimentary Research*, *70*, 1197–1209.
- 897 Ruan, Q., Zhang, Y., Yang, X., Nutt, S., & Moradian-Oldak, J. (2013). An amelogenin–chitosan  
898 matrix promotes assembly of an enamel-like layer with a dense interface. *Acta Biomaterialia*, *9*,  
899 7289–7297.
- 900 Ruttenberg, K. C. (2014). The global phosphorus cycle. In K. K. Turekian (Ed.), *Treatise on*  
901 *Geochemistry: Second Edition* (pp. 499–558). Oxford, UK: Elsevier.
- 902 Ruttenberg, K. C., & Berner, R. A. (1993). Authigenic apatite formation and burial in sediments  
903 from non-upwelling, continental margin environments. *Geochimica et Cosmochimica Acta*, *57*,  
904 991–1007.
- 905 Schenau, S. J., Slomp, C. P., & De Lange, G. J. (2000). Phosphogenesis and active phosphorite  
906 formation in sediments from the Arabian Sea oxygen minimum zone. *Marine Geology*, *169*, 1–  
907 20.
- 908 Schuffert, J. D., Kastner, M., & Jahnke, R. A. (1998). Carbon and phosphorus burial associated  
909 with modern phosphorite formation. *Marine Geology*, *146*, 21–31.
- 910 Schultze-Lam, S., Harauz, G., & Beveridge, T. J. (1992). Participation of a cyanobacterial Slayer  
911 in fine-grain mineral formation. *Journal of Bacteriology*, *174*, 7971–7981.

- 912 Schulz, H. N., & Schulz, H. D. (2005). Large sulfur bacteria and the formation of phosphorite.  
913 *Science*, *307*, 416–418.
- 914 Simon, P., Zahn, D., Lichte, H., & Kniep, R. (2006.) Intrinsic electric dipole fields and the  
915 induction of hierarchical form developments in fluorapatite–gelatine nanocomposites: A general  
916 principle for morphogenesis of biominerals? *Angewandte Chemie International Edition*, *45*,  
917 1911–1915.
- 918 Summerhayes, C. P., Birch, G. F., Rogers, J., & Dingle, R. V. (1973). Phosphate in sediments off  
919 South-western Africa. *Nature*, *243*, 509–511.
- 920 Titov, A. T., & Baturin, G. N. (2008). Microstructure and formation mechanism of calcium  
921 phosphate in recent phosphorites. *Doklady Earth Sciences*, *419*, 312–315.
- 922 Tourney, J., & Ngwenya, B. T. (2014). The role of bacterial extracellular polymeric substances in  
923 geomicrobiology. *Chemical Geology*, *386*, 115–132.
- 924 Tyrrell, T. (1999). The relative influences of nitrogen and phosphorus on oceanic primary  
925 production. *Nature*, *400*, 525–531.
- 926 Vallet-Regí, M., & González-Calbet, J. M. (2004). Calcium phosphates as substitution of bone  
927 tissues. *Progress in Solid State Chemistry*, *32*, 1–31.
- 928 Veeh, H. H., Burnett, W. C., & Soutar, A. (1973). Contemporary phosphorites on the continental  
929 margin of Peru. *Science*, *181*, 844–845.

- 930 Veeh, H. H., Calvert, S. E., & Price, N. B. (1974). Accumulation of uranium in sediments and  
931 phosphorites on the South West African shelf. *Marine Chemistry*, 2, 189–202.
- 932 Vinn, O., & Kirsimäe, K. (2014). Alleged Cnidarian *Sphenothallus* in the Late Ordovician of  
933 Baltica, Its mineral composition and microstructure. *Acta Palaeontologica Polonica*, 60, 1001–  
934 1008.
- 935 Voorhees, P. W. (1985). The theory of Ostwald ripening. *Journal of Statistical Physics*, 38, 231–  
936 252.
- 937 Watson, I., van Straaten, P., Katz, T., & Botha, L. (2014). Mining and concentration: What  
938 mining to what costs and benefits? In R. Scholz, A. Roy, F. Brand, D. Hellums, A. Ulrich (Eds.),  
939 *Sustainable Phosphorus Management. A Global Transdisciplinary Roadmap* (pp. 153–182).  
940 Dordrecht, the Netherlands: Springer.
- 941 Wu, Y.-J., Tseng, Y.-H., & Chan, J. C. C. (2010). Morphology control of fluorapatite crystallites  
942 by citrate ions. *Crystal Growth & Design*, 10, 4240–4242.
- 943 Zanin, Y. N., & Zamirailova, A. G. (2011). The history of the study of bacterial/cyanobacterial  
944 forms in phosphorites. *Russian Geology and Geophysics*, 52, 1134–1139.

945

## 946 **Figure captions**

- 947 **Figure 1.** Distribution of sediments on the southern part of the Namibian shelf with coring sites.  
948 Modified after Baturin (2000).

949 **Figure 2.** Optical micrograph of whole sediment: (a) core GC4 and (b) core 25005. Core 25005  
950 contains numerous fragile diatomaceous frustules. Scale bars represent 1 mm.

951 **Figure 3.** (a) characteristic XRD patterns of bulk sediment samples from cores GC4 (depth 10–  
952 11 cm) and 25005 (depth 4–5 cm). (b) apatite unit cell parameters for cores GC4 and 25005 in the  
953 context of different types of natural apatite. Modified after Nemliher (1999); Vinn & Kirsimäe  
954 (2014). (c) apatite and pyrite content in core GC4, XRD quantification; (d) apatite and pyrite  
955 content in core 25005; (e) phosphorus and sulfur content in core 25005, as measured by ICP-MS.

956 **Figure 4.** SEM-BSE overview images of whole sediment in (a) core GC4 and (b) core 25005.  
957 Both cores contain abundant apatitic pellets. SEM-SE images of single apatitic pellets from (c)  
958 core GC4 and (d) core 25005. Pellets from core GC4 tend to be larger and more rounded than  
959 those from core 25005. (e–f) SEM-SE images of broken surfaces of apatitic pellets from (a) core  
960 GC4 and (b) core 25005. Pellets from core 25005 contain much more pores and detritus.

961 **Figure 5.** SEM-BSE images of polished surface of the pellets: (a) core GC4 and (b) core 25005.  
962 Pellets from core GC4 display several 10–20  $\mu\text{m}$  thick rims, those from core 25005 usually have  
963 one, if any. (c) SEM-BSE image of a broken surface of a pellet, showing that the material is  
964 mainly composed of inter-grown radial microstructures (core 25005).

965 **Figure 6.** SEM-SE images of apatite particles from broken-surface pellets. (a) diverse forms of  
966 apatite microstructures (core 25005). (b) abundant apatite rod-shaped particles coat pore walls  
967 (core 25005). (c) rod-shaped particles in core 25005 are composed of anhedral apatite  
968 nanocrystallites oriented parallel to their long axis. Lighter in tone in the foreground is a spherical  
969 pyrite microaggregate. (d) apatite particles in core GC4 are composed of euhedral hexagonal

970 crystallites, oriented in the same manner as in panel c. (e) rod-shaped particles occur together  
971 with a film-like organic substance, seen here filling most of the image (core 25005). (f) rod-  
972 shaped particles often co-occur with framboidal pyrite (core GC4). Scale bars represent 1  $\mu\text{m}$ .

973 **Figure 7.** TEM images of intergrown rod-shaped apatite particles from core 25005. Large light  
974 bands on panels a, b, d–f and g, as well as the dark band covering the left half of panel h,  
975 represent carbon filaments, part of the lacy film that the FIB-cut is mounted on. (a, g) high-angle  
976 annular dark-field (HAADF) images of entire FIB-foils. (b) HAADF image illustrating the  
977 growth of rod-shaped particles in several concentric ~50–200 nm thick layers, originating from  
978 an ellipsoidal ~50–200 nm wide inner core, alternating between dense and porous. The layers are  
979 thickest at the distal ends of the particles. (c) HAADF image showing elongated apatite  
980 crystallites radiating along the long axis of the rod-shaped particles (some examples indicated by  
981 dashed lines). (d) HAADF image of a rod-shaped particle with layered internal structure; (e–f)  
982 overlaid Electron Energy Loss Spectroscopy jump ratio maps of carbon (i) and sulfur (j) of the  
983 same area. (h) bright field image of a rod-shaped particle. (i) Fast Fourier Transformed electron  
984 diffraction pattern of inner layer, showing greater crystallinity (sharp reflections). (j) Fast Fourier  
985 Transformed electron diffraction pattern of the outer layer of a rod-shaped particle, showing  
986 lower crystallinity (diffuse and smeared-out reflections).

987 **Figure 8.** SEM-SE images of broken-surface pellets (b from core GC4, all others from core  
988 25005). (a) rod-shaped apatite particles tend to intersect one another. (b) rod-shaped particles  
989 often form intergrown aggregates. (c) truncated apatitic particles, which appear to have nucleated  
990 tangentially on a pore wall (example of pore wall and apatitic particles is indicated by dashed

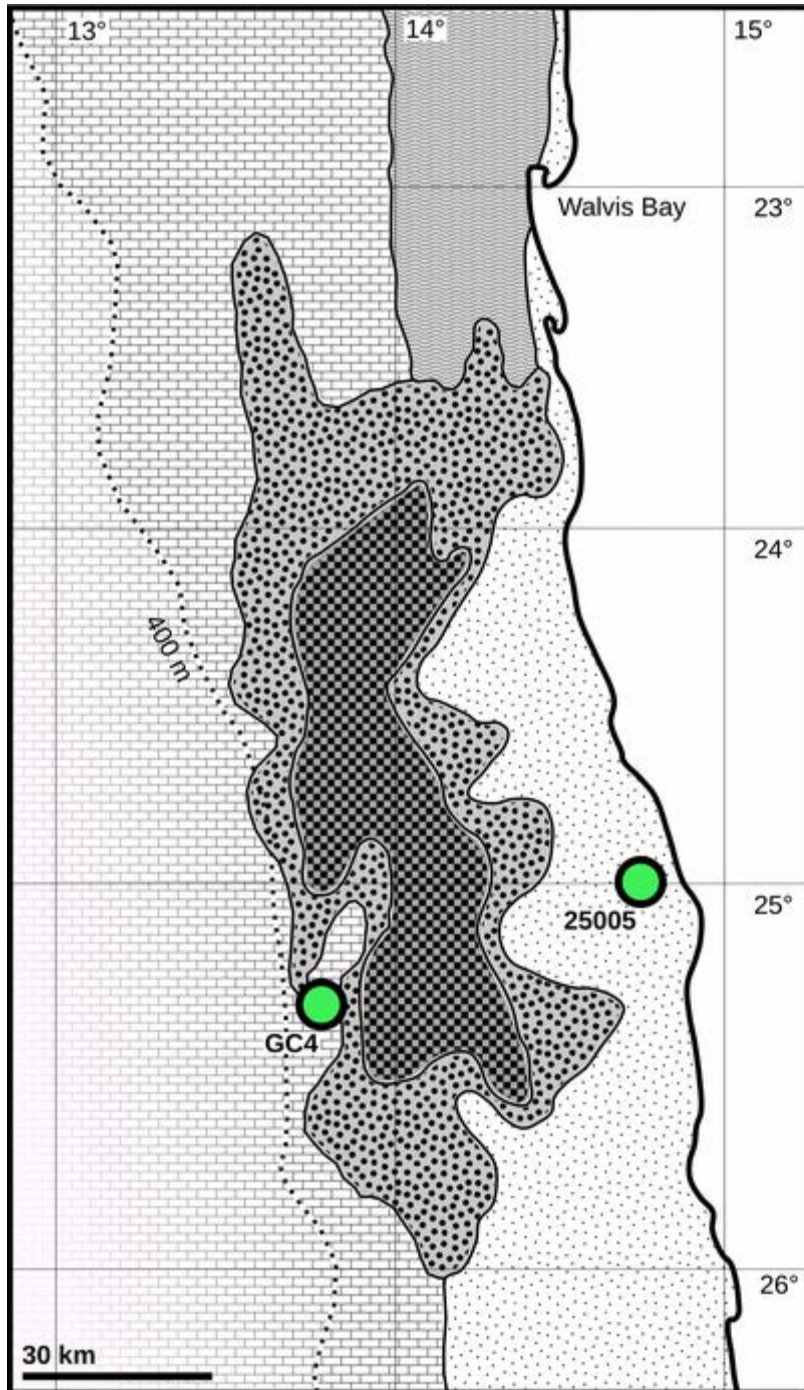




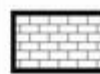



991 lines). (d) individual rod-shaped particles merge into the apatite matrix of the pellets. (e) rod- and  
992 dumbbell-shaped apatite particles display varying sizes. (f) spherical apatite particles. Scale bars  
993 represent 1  $\mu\text{m}$ .

994 **Figure 9.** SEM-SE (a,b,d) and SEM-BSE (c) images of progressing apatite growth forms from  
995 broken-surface pellets (c from core GC4, all others from core 25005). Rod-shaped and other  
996 apatite microstructures form a continuum from (a) spindle-shaped elongated rods to (b) rods that  
997 start to bulge at their distal ends to (c) dumbbells to (d) spherical particles. Scale bars represent 1  
998  $\mu\text{m}$ .

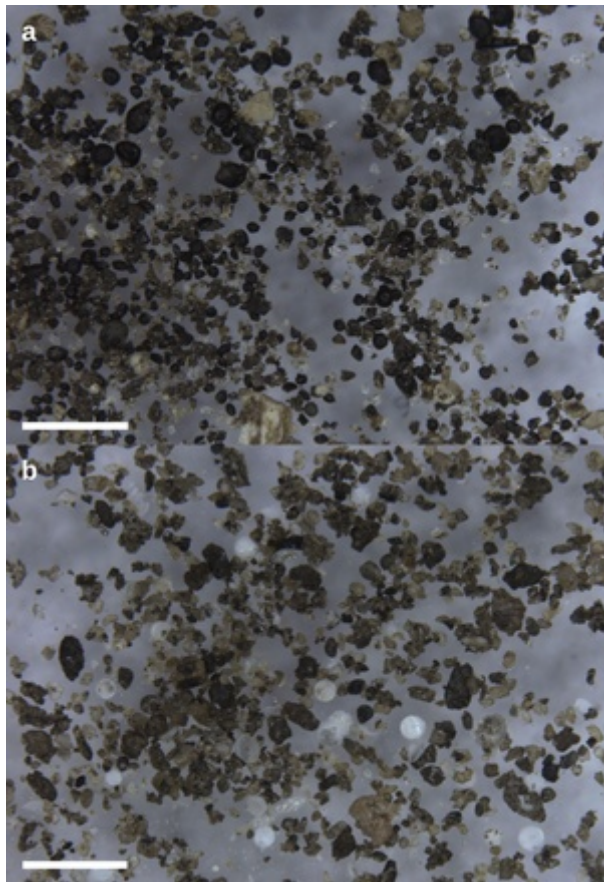
999 **Figure 10.** SEM images of apatite precipitated in organic matrices during double-diffusion  
1000 experiments (Crosby and Bailey, 2017; 2018). The resultant apatite morphologies range from (a)  
1001 spindle-shaped to (b) dumbbells to (c) spherical microstructures. Such apatite microstructures  
1002 often intersect and are composed of smaller lathe or hexagonal shaped apatite crystallites. (d–e) a  
1003 consortium of different apatite microstructures, concentrated in the harvesting phase. (f) apatite  
1004 overgrowth forming a 10–20  $\mu\text{m}$  thick radial layer over a laboratory-grown apatite sphere broken  
1005 to expose complex internal microstructures. Scale bars represent 10  $\mu\text{m}$ .

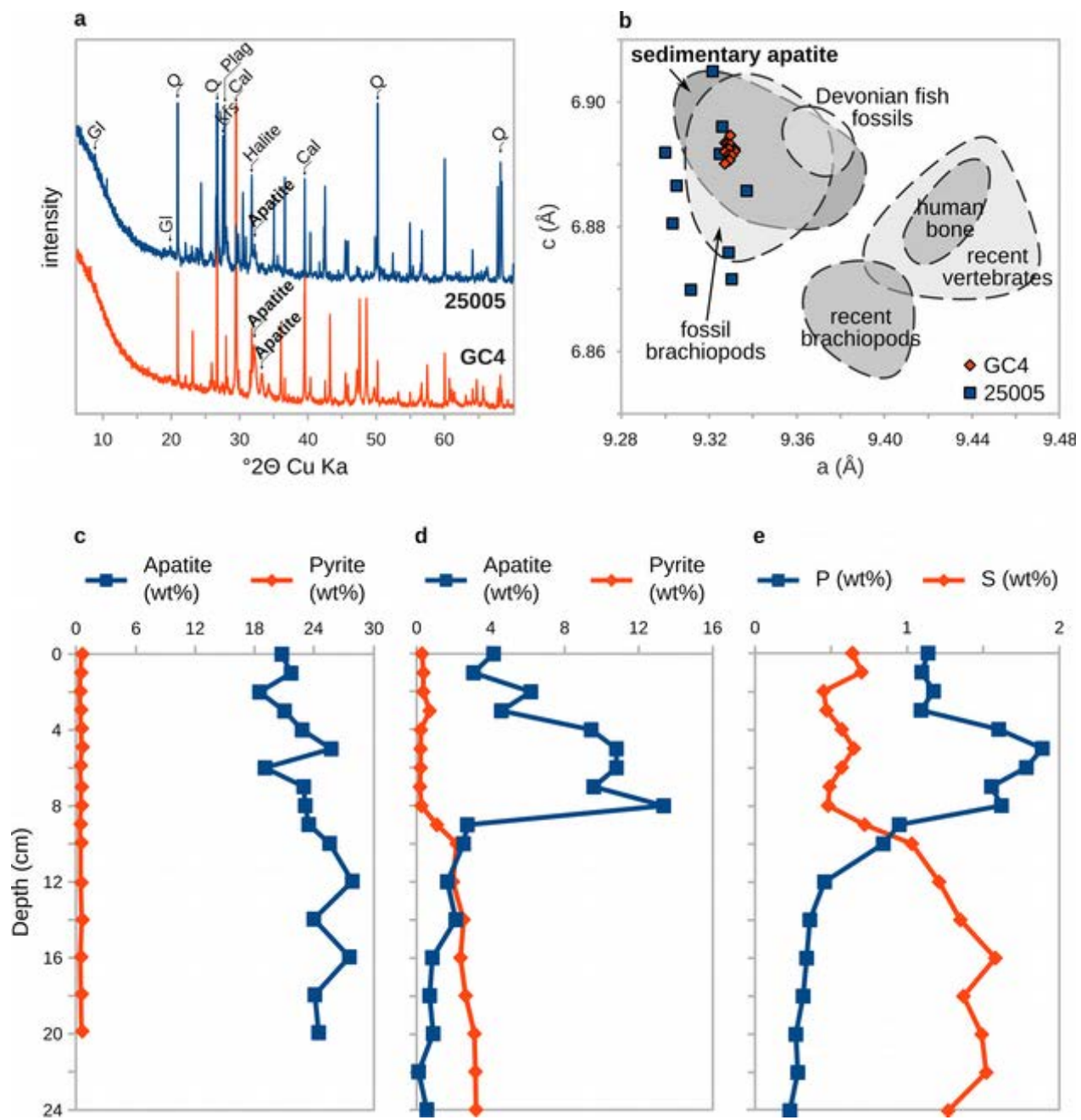
1006 Figure 1

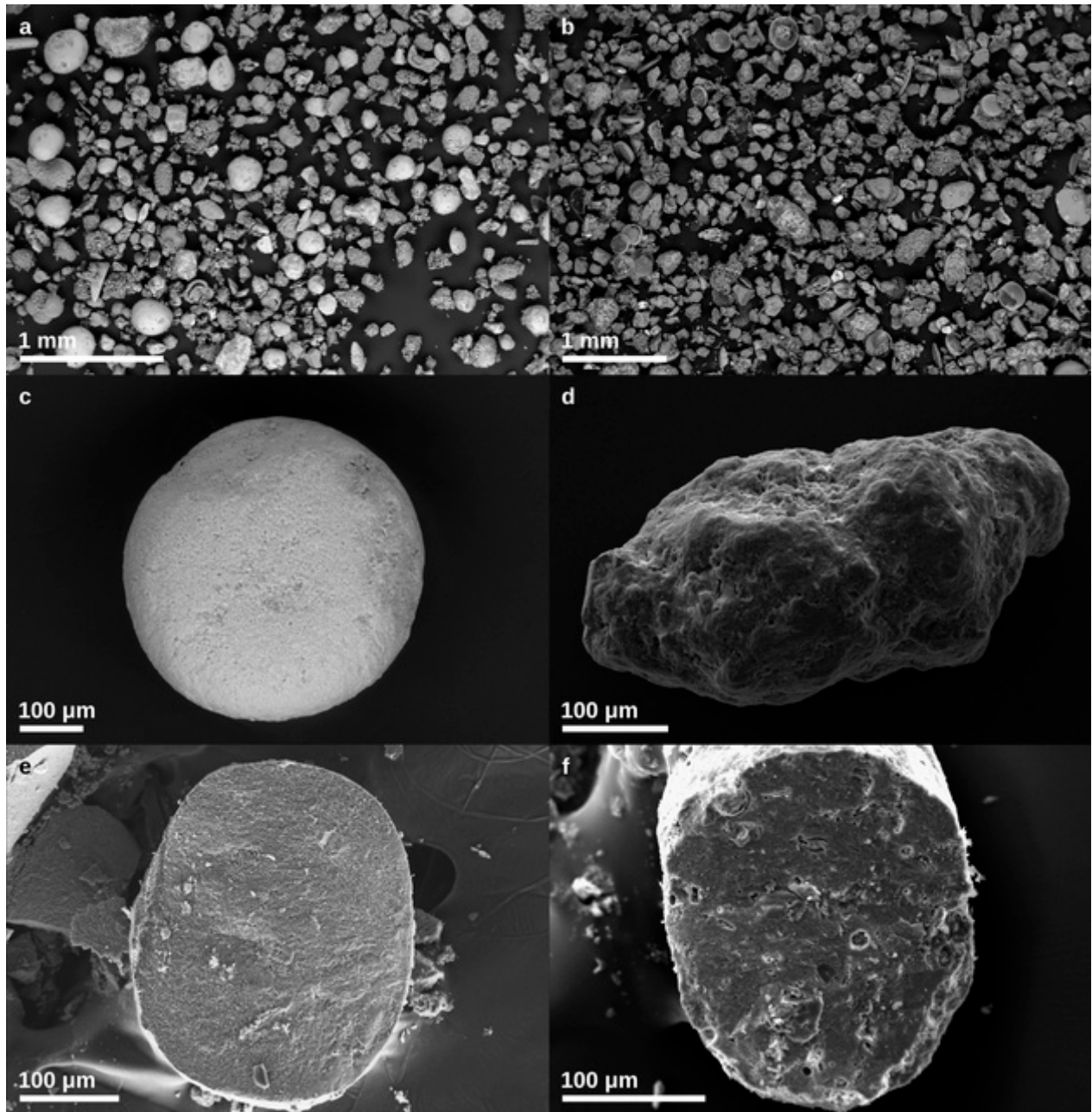


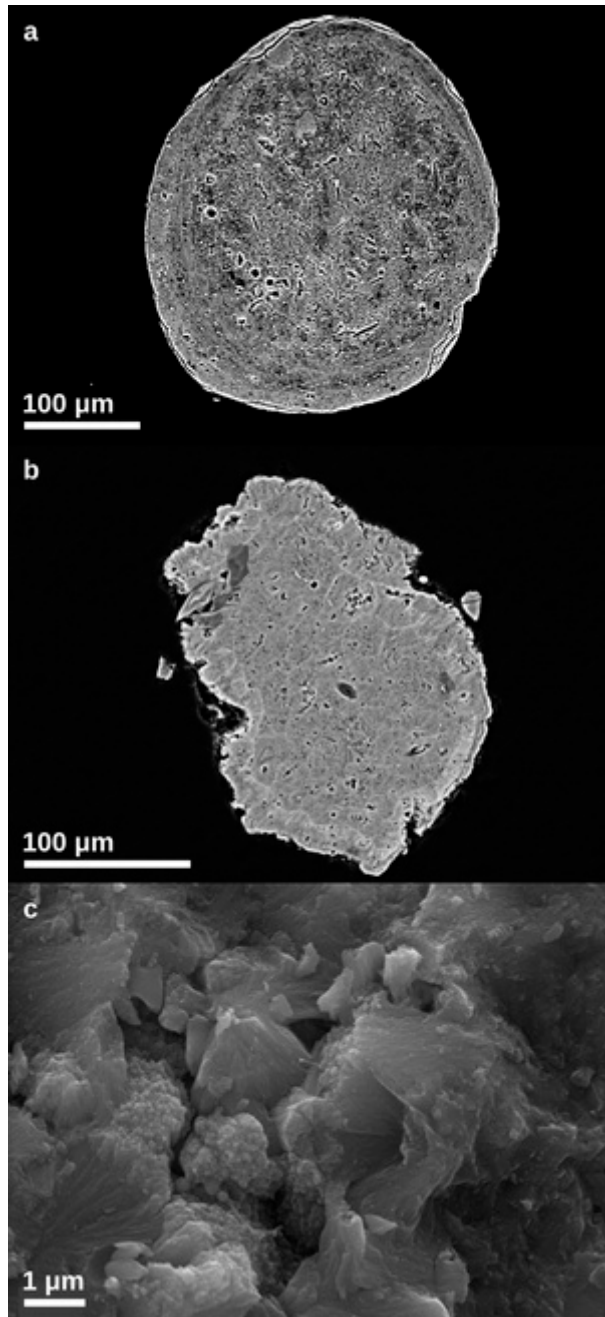
-  Coring site
-  Diatomaceous mud
-  Calcareous sediments
-  Shelly phosphatic sand
-  Phosphatic sand
-  Terrigenous sediments

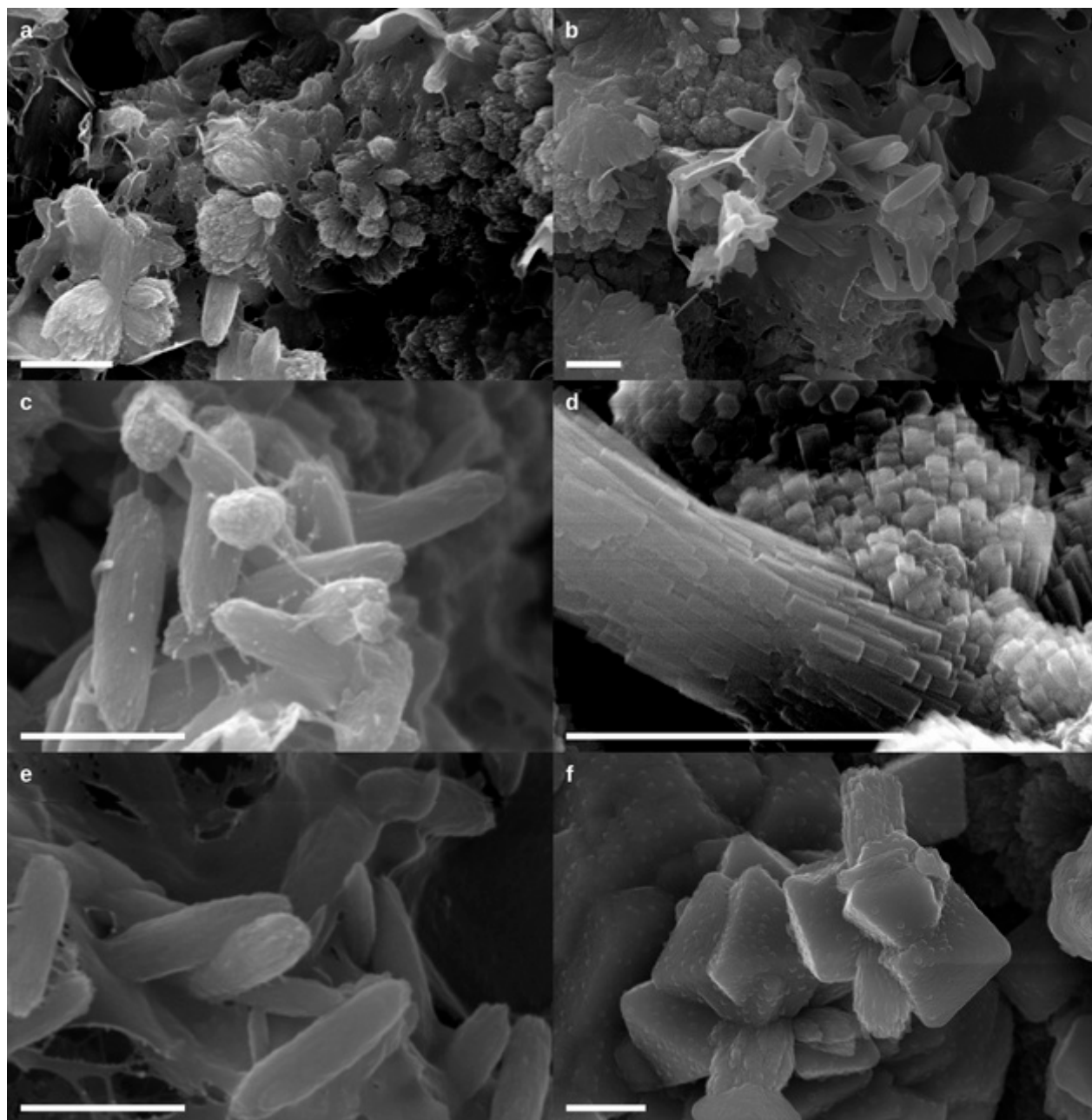
1007



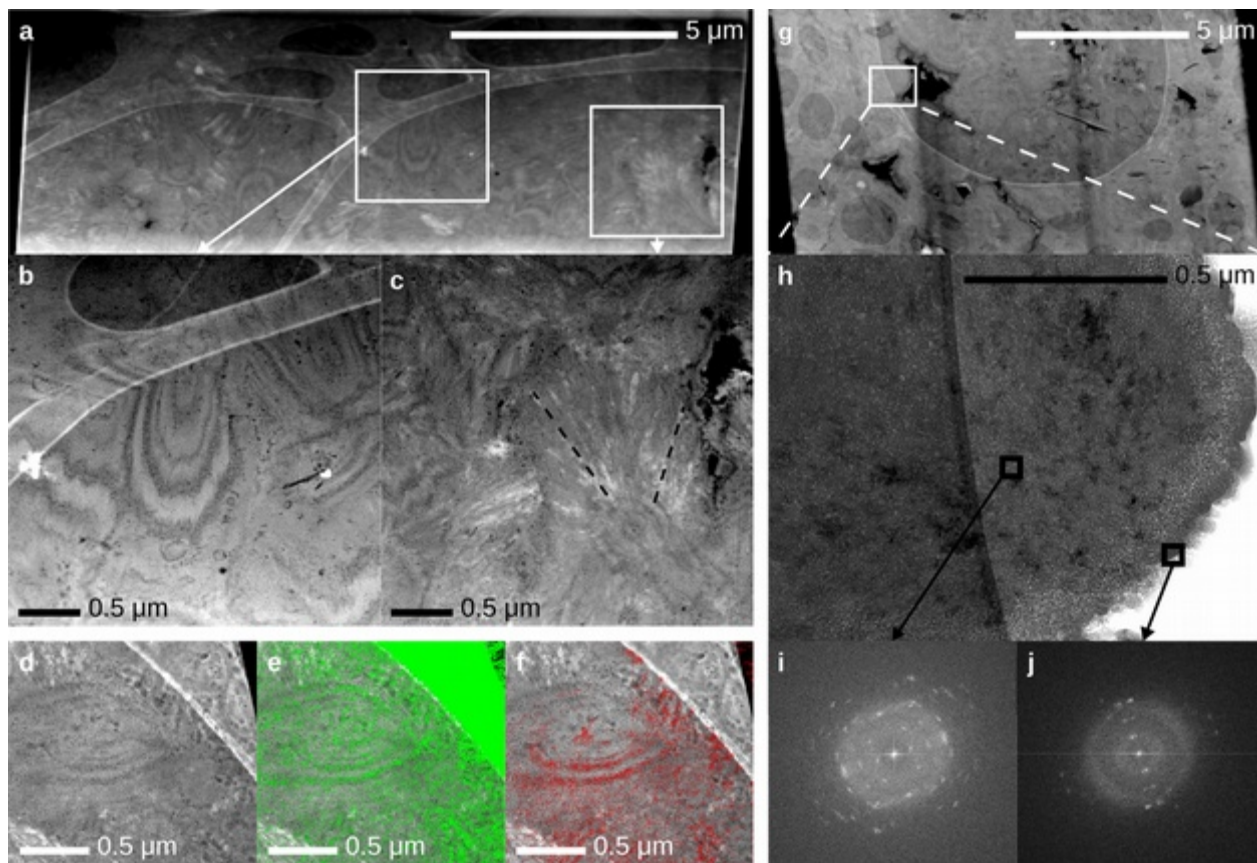






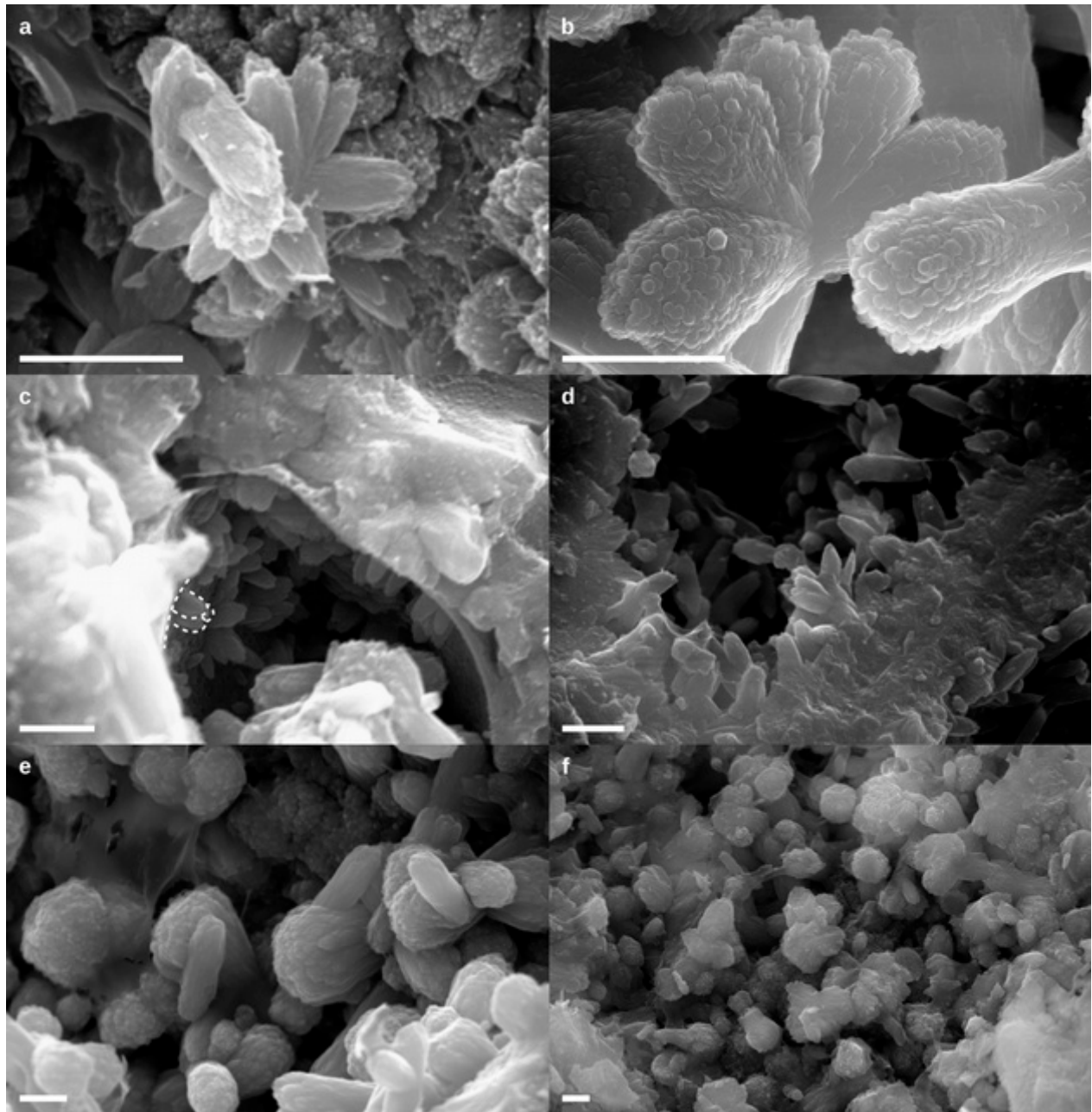


1018 Figure 7

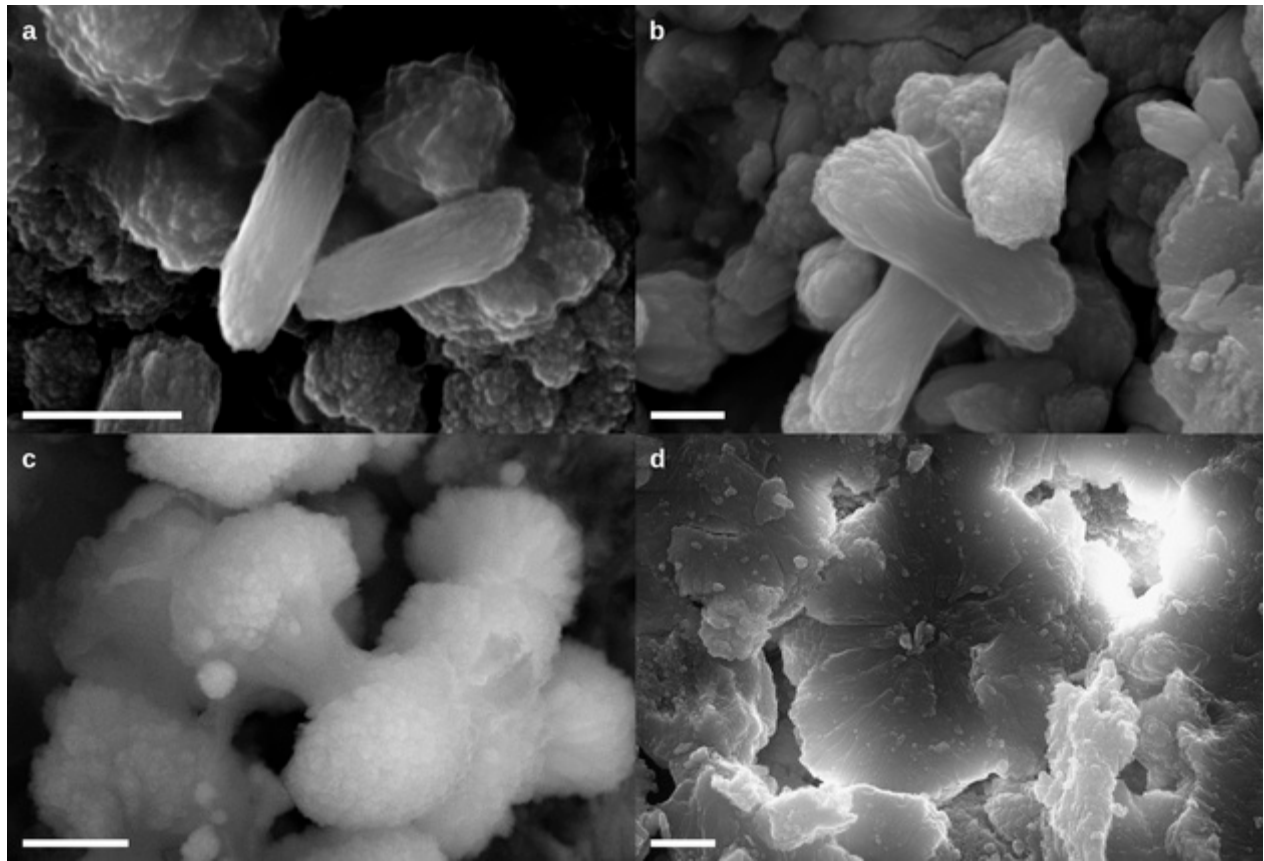


1019





1022 Figure 9



1023

